i

AMERICAN UNIVERSITY OF BEIRUT

DEFORMATION MECHANISMS IN MAGNESIUM SINGLE
CRYSTAL: MULTI-SCALE DISLOCATION DYNAMICS
ANALYSES

by
WASSIM ATEF JABER

A thesis
submitted in partial fulfillment of the requirements
for the degree of Master of Engineering
to the Department of Mechanical Engineering
of the Faculty of Engineering and Architecture
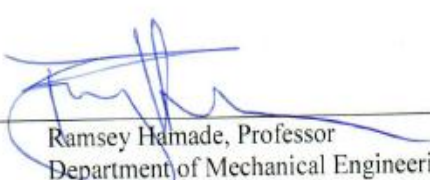at the American University of Beirut

Beirut, Lebanon
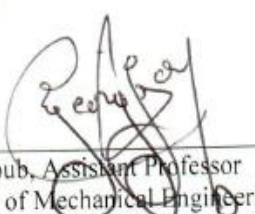April 27, 2015

AMERICAN UNIVERSITY OF BEIRUT

DEFORMATION MECHANISMS IN MAGNESIUM SINGLE
CRYSTAL: MULTI-SCALE DISLOCATION DYNAMICS
ANALYSES

by
WASSIM ATEF JABER

Approved by:

_____   Advisor
Mu'tasem Shehadeh, Assistant Professor
Department of Mechanical Engineering

_____   Member of Committee
Ramsey Hamade, Professor
Department of Mechanical Engineering

_____   Member of Committee
George Ayoub, Assistant Professor
Department of Mechanical Engineering

29 - April - 2015

Date of thesis defense: April 27, 2015

iii

AMERICAN UNIVERSITY OF BEIRUT

THESIS, DISSERTATION, PROJECT RELEASE FORM

Student Name:_____
           Last   First   Middle

◯ Master's Thesis   ◯ Master's Project   ◯ Doctoral
Dissertation

☐   I authorize the American University of Beirut to: (a) reproduce hard or
electronic copies of my thesis, dissertation, or project; (b) include such copies in the
archives and digital repositories of the University; and (c) make freely available such
copies to third parties for research or educational purposes.

☐   I authorize the American University of Beirut, **three years after the date of
submitting my thesis, dissertation, or project,** to: (a) reproduce hard or electronic
copies of it; (b) include such copies in the archives and digital repositories of the
University; and (c) make freely available such copies to third parties for research or
educational purposes.

_____

Signature   Date

ACKNOWLEDGMENTS

AN ABSTRACT OF THE THESIS OF

Wassim Atef Jaber   for   Master of Engineering
                                                   <u>Major</u>: Mechanical Engineering

Title: <u>Deformation mechanisms in magnesium single crystal: multi-scale dislocation
dynamics analyses.</u>

Hexagonal-closed packed materials (HCP) materials has attracted interest recently due to their unique physical and mechanical properties. The low density and the high strength to weight ratio of such materials make them excellent candidates to save structural weight and consequently fuel consumption in both automotive and aircraft fields. However, the deformation behavior of HCP metals hasn't been completely understood as prior work still lack a detailed understanding on the activation of slip planes and twinning. In addition, the work-hardening behavior and the effect of size and strain rate are not yet well-established. This work aims at investigating the deformation mechanisms in magnesium single crystals using Multiscale Dislocation Dynamics Plasticity (MDDP) model. In particular, we focus on studying the effect of dislocation mobility dependence on the dislocation character and on modeling the deformation behavior under different orientations, and for different sizes, strain rates and loading conditions. Our results show that the experimentally observed hardening behavior can be reproduced by using linear interpolation of the mobility such that screw segments are stationary and edge segments are highly mobile. In addition, simulations for size effect, on yield stress and hardening behavior, for finite crystal are in good agreement with recent experimental results. Also, a one fourth power law exponent, similar to the one developed by Swegle & Grady (1985) was obtained for the variation of the strain rate with yield stress. Moreover, shock loading results are consistent with recently published experiments regarding particle velocity history, and the stress profile. These findings provide a better understanding of the complicated plastic deformation in HCP crystals, in particular, Mg single crystals.

CONTENTS

ILLUSTRATIONS

TABLES

Chapter I

INTRODUCTION

A. Rationale

In recent years, Hexagonal Close-Packed (HCP) materials such as Magnesium (Mg), titanium and their alloys have attracted the attention of many research groups. Due to the ever increasing need for energy efficiency, the search for lightweight material is an active area of research. Mg, the lightest of all metals, provides great promise, and induce automotive and aircraft fields to replace denser materials (i.e. steel alloys) with Mg-based alloys. Magnesium's c/a ratio (1.624) is close to the ideal HCP crystal's ratio of 1.633, making it a good representative element for research studies on HCP materials. Furthermore, Mg is considered to be highly recyclable, possess good machinability, and have a high damping capacity and a low melting temperature [1]. In addition, Mg alloys have been also used in electronic and biomedical applications due to their electromagnetic shielding capability and biocompatibility [2]. Despite having many attractive properties, plastic anisotropy and the relatively low ductility influence the use of magnesium as a structural member. Table 1 is a summary of the important physical properties of Magnesium.

While most of the investigations of the deformation mechanism in metals have been focused on Face-Centered Cubic (FCC) and Body-Centered Cubic (BCC) structures, little work has been performed on HCP structured materials. Due to their low symmetry, the deformation behavior is much more complicated than that of high symmetry FCC metals. Even though there was an increase in their technological applications recently, many fundamental problems remain open; i.e. the identification of the active slip systems, work-hardening behavior and strain rate dependence. A detailed understanding of the relationship between the microstructure of HCP metals and their mechanical properties such as yielding

strength, toughness, and hardening laws, is very crucial in the design of HCP based

components.

Table 1: Important Physical Properties of Magnesium

Property	Value
Elastic Modulus	45 GPa
Poisson Ratio	0.33
Shear Modulus	16.9 GPa
Density	1740 kg/m^3
c/a ratio	1.624

B. Crystallography

All real crystals contain imperfections which may be point, line, surface or volume

defects, and which disturb locally the regular arrangement of the atoms. According to the

dislocation theory, plastic deformation in crystals is achieved by the generation and transport

of dislocations as shown in figure 1. A dislocation is a line defect within a crystal structure

such that its presence can significantly modify the properties of crystalline solids.

Geometrically a dislocation line is defined by its Burgers vector (b) and line sense (ξ). The

Burgers vector is the displacement of the atoms that occurs in the crystal as the dislocation

moves. The line sense is a unit vector tangent to the dislocation line. When the Burgers vector

is normal to the line sense the dislocation is defined as edge dislocation and when it is

parallel to the line sense it is defined as screw dislocation. The dislocation can be a line

extending until it reaches a free surface or an interface or it can be a closed loop within the

crystal. As the dislocation is a line defect, it is associated with an internal strain field that

varies as the inverse of the distance from its core [3]. Burgers vectors for the HCP structured

materials may be described in a similar fashion to the Thompson tetrahedron for face-

centered cubic metals by using the bi-pyramid model shown in figure 2. The perfect

dislocations in the figure are represented by their Burgers vectors as follows:

- Perfect Dislocation with one of 3 Burgers vectors <a>: one of the triangular

  base ABC (AB-BC-AC)

- Perfect Dislocation with Burgers vector <c>: perpendicular to basal plane,

  represented by ST-TS

- Perfect Dislocation with one of 6 Burgers vector <c+a>: is the combination of

  vectors AB/ST or their equivalent.
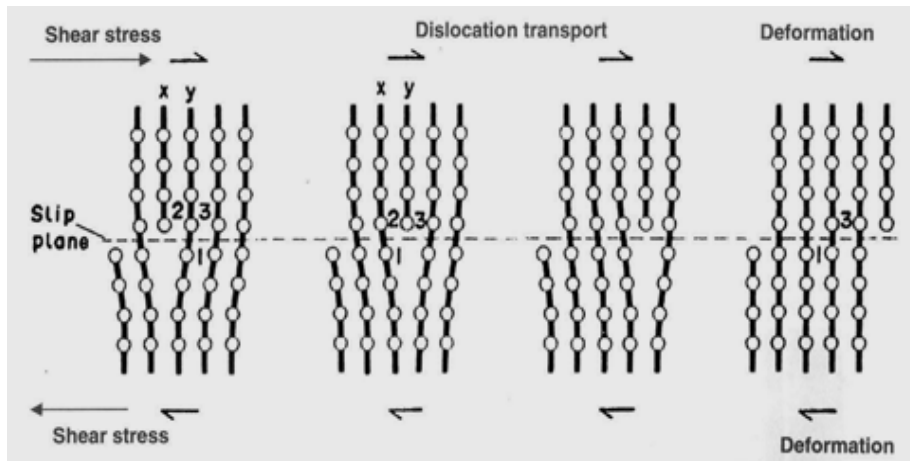
Figure 1: Dislocation motion in the crystal lattice
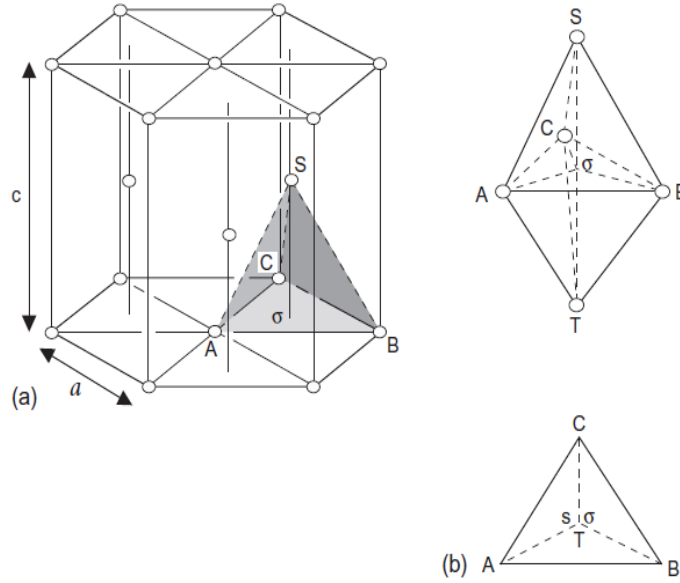
Figure 2: Burger vectors in hexagonal close-packed lattice [3]

C. Literature Review

Slip and twinning emerge as the two main deformation modes in HCP metals. Figure 3 shows the common slip and twinning planes. For slip, the basal, prismatic and pyramidal $\pi 1$ slip systems have <a> Burgers vector, whereas the pyramidal $\pi 2$ slip system has <c+a> Burgers vector. Regarding the <c> dislocation, it is a sessile dislocation, thus it cannot contribute to the deformation and is not considered as an important slip system [4]. Table 2 provides a summary for the available slip system in HCP materials, with the corresponding slip planes and slip directions. Regarding twinning in HCP materials, it is very dependent on orientation and (c/a) ratio: As for orientation, $\{11\bar{2}1\}$, $\{11\bar{2}4\}$, $\{10\bar{1}3\}\}$ twin planes are observed for c-axis compression, while $\{11\bar{2}2\}$ and $\{10\bar{1}1\}$ are tension twins. The most common twinning system that occurs in almost all HCP metals is the tensile twinning system $\{10\bar{1}2\}$ <$10\bar{1}1$>. It occurs in compression for cadmium and zinc, and in tension for all other HCP metals. It is noted that the twinning systems in the <$11\bar{2}0$> zone are either tensile twinning $\{10\bar{1}2\}$, or compressive twinning $\{10\bar{1}1\}$ and $\{10\bar{1}3\}$. Regarding c/a ratio, if this ratio is lower than $\sqrt{3}$, twinning is favored by compression normal to the c-axis and tension parallel to the c-axis. In

4

contrast, for c/a ratio greater than √3, compression parallel to the c-axis and tension normal to the c-axis favor twinning [4].
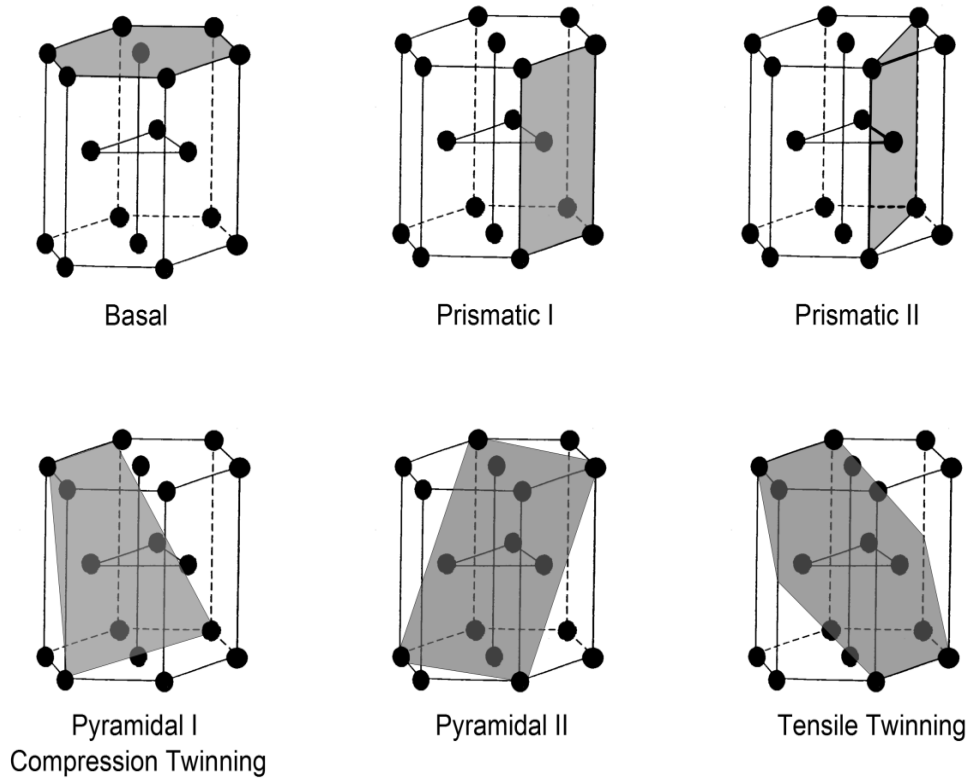
Figure 3: Common Slip and Twinning Planes in HCP materials

Table 2: Potential sip systems in hcp materials [4]

Slip System	Slip System Type	Burgers Vector Type	Slip direction	Slip Plane	Number of Slip Systems	
					Total	Independent
1	Basal	a	$<11\bar{2}0>$	(0001)	3	2
2	Prism 1	a	$<11\bar{2}0>$	$\{10\bar{1}0\}$	3	2
3	Pyramidal 1	a	$<11\bar{2}0>$	$\{10\bar{1}1\}$	6	4
4	Pyramidal 2	c+a	$<11\bar{2}3>$	$\{11\bar{2}2\}$	6	5
5	Prism 1	c	$<0001>$	$\{10\bar{1}0\}$	3	2
6	Prism 2	c	$<0001>$	$\{11\bar{2}0\}$	3	2

1. Basal Slip

Due to the high anisotropy exhibited by HCP metals, the stress required to activate their deformation modes is very dependent on the orientation. In magnesium, the basal slip of Burgers vector <a> is known to be the easiest system at all temperatures. This is also true for metals with c/a ratios higher than the ideal one; i.e. cadmium and zinc. As c/a ratio decreases, for example in titanium, prismatic slip becomes more dominant compared to basal slip as the prismatic planes become more closely packed than basal ones. Initial studies on magnesium single crystals indicate that, when the basal plane is within 6°-72° to the tensile axis of the samples, basal slip is the sole operative deformation mode [5]. Wonsiewicz and Backofen [6] have conducted plane strain compression experiments on single-crystal Mg and observed that c-axis strains are accommodated by double twinning along the $\{10\bar{1}1\}$- $\{10\bar{1}2\}$ planes followed by basal slip within the twinned regions. Hirsch and Lally [7] revealed the activation of basal slip in magnesium single crystals at room temperature by transmission electron microscopy (TEM). The reported shear stress-strain curve exhibit two distinct stage: the first one is an easy glide region characterized by low work hardening rate as most of the dislocation annihilate or form dipoles. Strong work hardening rate was observed at the second stage due to intersection of dislocations in the basal plane.

More recently, Kim [8] performed microcompression tests on magnesium single crystal samples in the $[2\bar{1}\bar{1}2]$ and $[10\bar{1}1]$ directions (the so-called 45° orientation). A large number of <a> type dislocations were observed, indicating the dominance of basal slip, with no signs of twins. The stress-strain curves show that yielding occur at 20-30 MPa with a nearly perfect plastic behavior. Furthermore, magnesium single crystal samples with initial orientation of $[2\bar{1}\bar{1}2]$ were tested, at room temperature and below, by Bhattacharya et al. [9]. They reported a CRSS of 1-1.5 MPa in the temperature range of 4.2 K to room temperature, which is close to the previously reported values of 0.5 [5,7] and 0.8 [10]. Extensive

elongation was reported with engineering strain up to 200%. The samples showed two-stage work hardening; the first easy glide stage was followed by rapid hardening. TEM observations at the easy glide stage reveal a huge number of dislocation substructures that correspond to the basal slip plane while the latter stage was attributed to the activation of the non-basal slip systems.

In addition, Prasad et al. [11] studied magnesium single crystals with orientation of $[2\bar{1}\bar{1}2]$ for two sample sizes ranging from mm to μm. A significant size effect was observed in the flow stress and the strain hardening behavior. Figure 4 shows the obtained stress-strain curves. The reported CRSS for micropillars (30 MPa) was higher than the bulk samples (5 MPa). In addition, the stress strain curve for the bulk samples was smooth and show slight strain hardening that is attributed to the large number of mobile dislocations resulting in forest hardening. In contrast, micropillar's stress strain curve exhibit several load drops that coincide with glide along a set of basal planes. Aitken et al. [12] conducted uniaxial compression experiments on single crystalline magnesium alloy AZ31 nanopillars with diameters 850 nm to 2100 nm oriented, at an acute angle to the c-axis, for basal slip. The deformation behavior was observed to be via a single set of parallel basal planes. The stress-strain curve for the sub-micron samples show negligible hardening with an "easy plastic" plastic flow. The bigger sample showed an increase of stress with deformation, as dislocations are more likely to interact with other dislocations or obstacles.
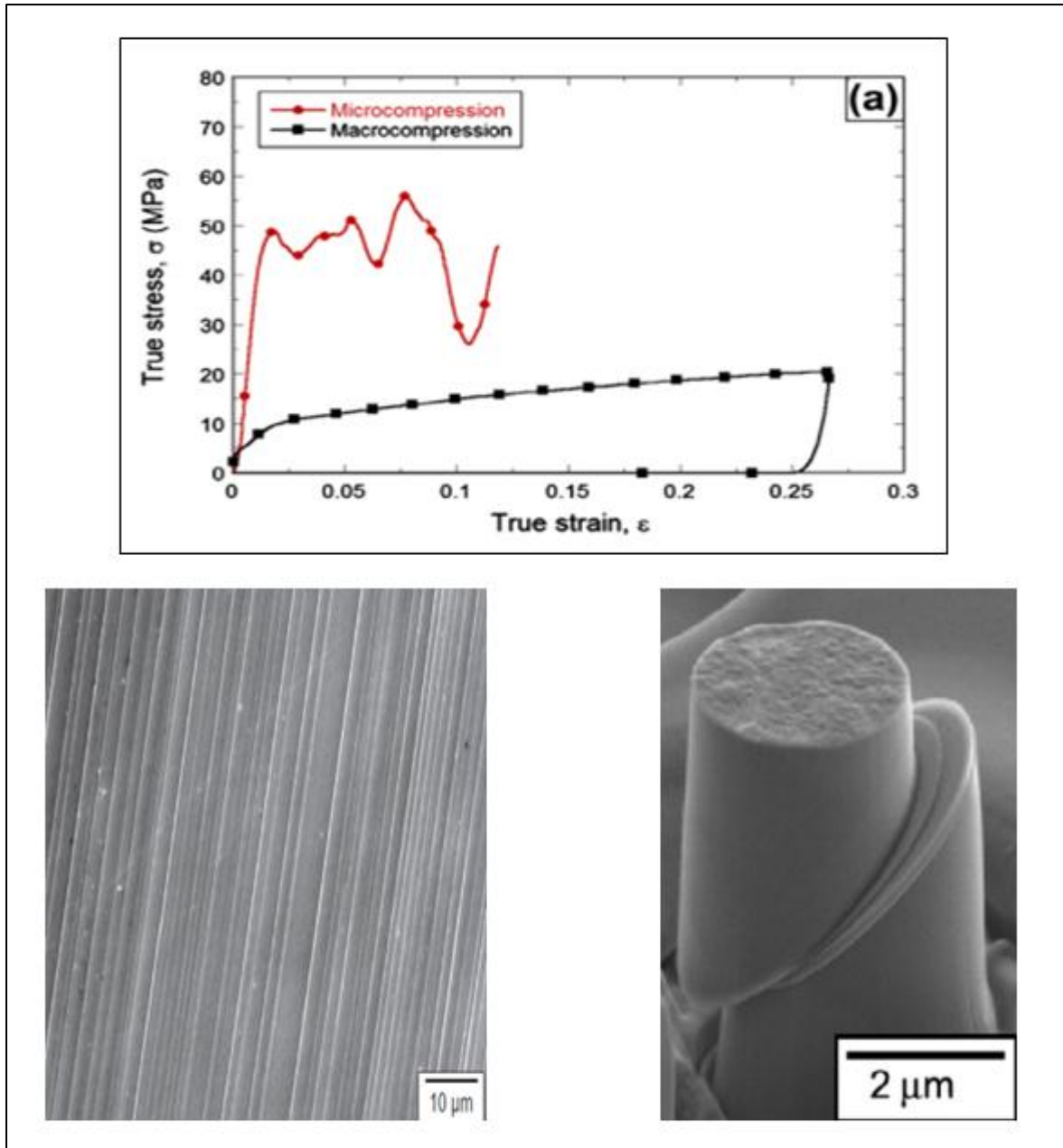
Figure 4: Stress-Strain curve of microcompression and macrocompression tests and deformation behavior [11]

2. Non-Basal Slip

Other experiments investigated non-basal slip in HCP materials. In one orientation that was designed to inhibit basal glide, Couret et al. [13] revealed traces of <a> dislocations on prismatic planes for a temperature range of 50 K – 650 K. Also, $<10\bar{1}0>$ oriented magnesium single crystals showed activity of prismatic I $\{10\bar{1}0\}$ $<11\bar{2}0>$ slip system for low temperature range and pyramidal 1 $\{10\bar{1}1\}$ $<11\bar{2}0>$ slip system at elevated temperatures [14].

This was in contrast to the work of Burke et al. [5] who reported occurrence of pyramidal I slip system in magnesium at room temperature when the basal plane was parallel to the loading axis. In a contrasting result to [14], compression along the $<11\bar{2}0>$ and $<10\bar{1}0>$ directions, by Molodov et al. [15], led to activation of $\{10\bar{1}2\}$ extension twinning. The resultant new orientation of the $<11\bar{2}0>$ compression was favorable for basal slip and further $\{10\bar{1}2\}$ twinning, while the second orientation didn't and failed at low strain. More recently, when the loading axis was inclined 10^{0} to the c-axis, Li [16] observed prismatic I $\{10\bar{1}0\}$ $<11\bar{2}0>$ slip system for magnesium single crystals samples.

To accommodate plastic deformation in the c-axis direction and to fulfill Von-Mises criterion for homogenous deformation of polycrystalline deformation, non-basal slip planes are necessary to provide five independent slip systems [17]. Several experimental studies on the deformation behavior of single crystal magnesium for c-axis compression and a-axis tension have been carried out. Many studies reported <c+a> pyramidal II slip system as the solo governing deformation mode [8, 18, 19, 20, 21, 22, 24], while other studies observed $\{10\bar{1}1\}$ compression twinning [6, 10, 15], with some reports about the occurrence of both deformation mechanisms [16, 25, 26, 27]. In the early seventies, Obara et al. and Stohr et al. [18, 19] observed pyramidal II slip system for a wide range of temperatures using Transmission Electron Microscopy (TEM) images. However, Chapuis et al. [25] observed the occurrence of pyramidal slip only above 450°C. These contrasting results may be related to the different loading conditions used as Chapuis et al. [25] used channel die compression while Obara et al. [18] used uniaxial compression. The obtained stress-strain curves by Obara et al. [18] showed a strong work hardening rate, especially below 200°C. They suggested that the exhaustion of highly mobile screw dislocations in early stages of deformation is the reason behind the high work-hardening rate. On the other hand, Yoshinga et al. [10] reported

9

basal and prismatic slip acting as accommodation mechanisms for $\{10\bar{1}1\}$ compression twinning. The reported absence of any pyramidal II slip was attributed to the high CRSS of that system compared to lower CRSS of compression twinning. A-axis tension and c-axis compression of samples were loaded for a wide range of temperatures (77K-573K) by Ando et al. [24]. They observed yielding due to Pyramidal II $\{11\bar{2}2\}$ <$11\bar{2}3$> slip system, with the yield stress in compression higher than that of tension. In other experiments [15], Plane Strain Compression (PSC) of magnesium single crystals, along the c-axis, resulted in premature failure at very low strain. This observed poor formability was attributed to initial hard orientation and lack of active deformation mechanisms. A sample of c-axis compression experiments showing pyramidal slip is shown below in figure 5.
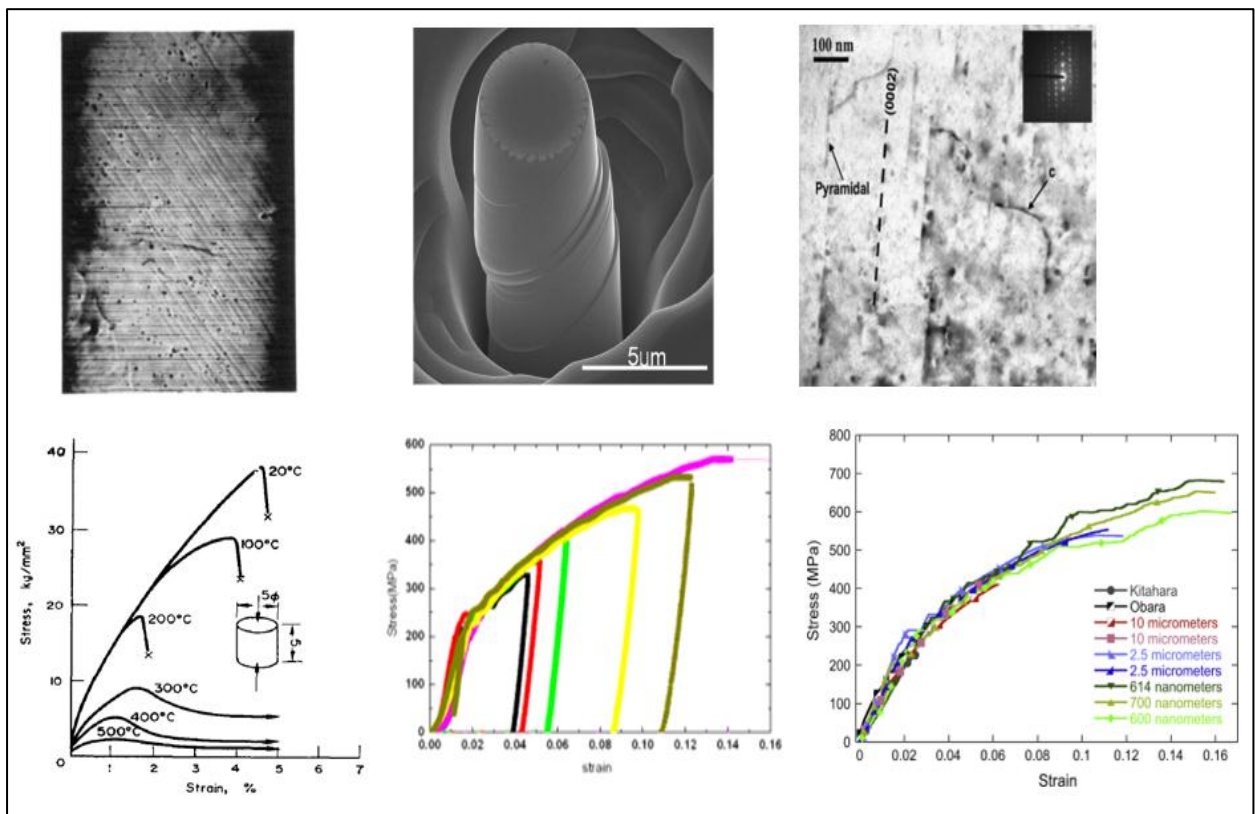
Figure 5: [0 0 0 1] compression experiments showing pyramidal slip [8] [18] [20]

More recently, Li [16, 26] conducted ambient compression loading experiments on magnesium single crystals with their [0001] direction about 10° away from the loading direction. In addition to activation of prismatic <a> and pyramidal II <c+a> slip system, the observed $\{10\bar{1}2\}$ tensile twins refined the sample to become polycrystalline. Moreover, pyramidal II slip system is found to be the main operative system below ambient temperature in magnesium-lithium alloy [23]. Kim [8] did micro-compression tests on magnesium single crystal and observed strong hardening behavior due to the activation and multiplication of <c+a>dislocations on the six pyramidal II glide planes. In addition to dislocation interaction, junction formation between <a> and <c+a> dislocations was observed, and is thought to be the reason for hardening. The local misorientation in the sample, resulting from plasticity, activated the basal slip system leading to a massive strain burst [8]. Byer et al. , Lilloledin et al. and Syed et al. [20, 21, 27] performed similar tests and reported activation of pyramidal II <c+a> slip system with no deformation twins as observed by kim [8]. This is in agreement with Syed et al. [27] who suggested that twinning could not be the major form of deformation for this orientation, as the density of twins is low compared to the slip.

The temperature effect of the deformation process of magnesium has been studied for basal and non-basal orientations. For basal orientation, it was reported that as the temperature decreases, the yield stress increases and fracture occurs at lower strains. In contrast to basal slip, samples loaded for pyramidal II slip exhibit anomalous flow stress behavior for different temperatures. This was attributed to the nature of <c+a> dislocations which may dissociate into glissile and sessile dislocations depending on temperature [6, 16, 25].

In addition to experimental investigations, few simulation approaches has been used to understand the deformation behavior of HCP materials. Monnet et al. [28] performed DD simulations of single crystals zirconium for prismatic glide. Kim [8] used DD to simulate

11

deformation behavior of single-crystal magnesium loaded at [0001] orientation in compression. After dislocation multiplication, only one or two slip planes of the six pyramidal II slip planes glided intensively, producing a crystal reorientation that leads to the activation of basal slip. However, Kim [8] was not able to reproduce the hardening behavior observed in experiments. MD simulations of c-axis compression in nanoscale magnesium single crystals showed that pyramidal II slip dominates, with no compression twins observed at different temperatures, different loadings and boundary conditions [29]. Gue et al. [29] proposed that the $\{10\bar{1}2\}$ and $\{10\bar{1}1\}$ twins can be activated under c-axis tension, while compression twins will not occur when the c/a ratio of the HCP metal is below $\sqrt{3}$.

3. Mobility anisotropy

The unusually high work-hardening rate present in Mg for c-axis compression is quite interesting. A possible explanation for such a behavior is in the presence of sessile <c+a> dislocation loops at the basal plane. These loops were previously reported by Stohr et al. [19]. Kumar et al. [30] argued that the mobile screw dislocations intersect other moving screw and stationary edge dislocations, creating jogs that contribute to the work-hardening behavior. Previously, Obara et al. [18] observed that screw dislocations have higher mobility than edge ones. On the other hand, Groh et al. [31] have revealed strong anisotropies in dislocation mobility values between slip modes and dislocations characters. Using molecular statics and molecular dynamics, they calculated these values at 100 K with an overall higher drag coefficient for the screw component which implies a higher edge dislocation mobility than screw ones. An in situ TEM experiments by Caillard et al. [32] revealed presence of long screw segments which suggests a significant anisotropy for lattice friction and mobility of such dislocations. The ratio of mobility of edge segments over screw ones was taken to be a thousand by Capolungo et al. [33]. This ratio is similar to the one taken for prismatic planes

12

in Zirconium (Zr) by [34]. Using Density Functional Theory (DFT), Ghazisaeidi et al. [35] studied the core structures of <c+a> dislocations on the pyramidal II planes. They revealed that the CRSS required for gliding of screw dislocation is higher than that of edge one. Previously, Carter et al. [36] showed similar anisotropy for prismatic planes. Amid conflicting reports about the anisotropy in the dislocation mobility and frictional stress values depending on dislocation character, it is vital to further investigate this issue.

4. Shock Loading

High strain rate processes refer to events in which the material is subjected to a rapid deposition or transmission of energy in a small region through the propagation of shock waves. Shock waves are supersonic disturbances that lead to large changes in pressure (compression), density and internal energy almost instantaneously. The time over which the material can achieve these abrupt changes ranges between hundreds of nanoseconds to fractions of nanoseconds depending on the extremity of the loading condition.

Shock waves can be generated by different means such as mechanical from high-speed impact, chemical from explosives, radiative from high intensity laser or nuclear from neutrons. Shock waves can propagate in one, two or three dimensional geometries, however most of the research attention has been focused on the propagation of one dimensional wave, as it is extremely difficult to carry out precise measurements in two and three dimensional geometries. Under shock loading condition, the material undergoes changes in its mechanical, physical and mechanical properties. In solid mechanics, we are mainly interested in developing fundamental understanding of the material response under extreme conditions and the deformation process accompanied by shock propagation. By that we can improve our understanding to the deformation process under extreme conditions and design novel materials with enhanced mechanical properties.

The ideal shock profile (exhibited by normal fluids) consists of a discontinuous shock front, plateau at the peak pressure whose duration is equivalent to the pulse duration and a release part as shown in figure 6a. This kind of idealization is used when the behavior of the solid material is assumed to be fluid like. In real solids however, the wave profile is different as different peculiarities are exhibited such as plastic deformation. Shock waves are usually classified as weak, moderate and strong. When the shock strength exceeds the critical value of plastic flow stress defined as the Hugoniot elastic limit (HEL), yielding phenomenon occurs and leaves elastic precursor that separates the elastic and plastic regimes on the wave profile (See figure 6). It is worth mentioning that although the HEL in metals is low, it can be very high in ceramics; take for example sapphire where HEL ~ 20 GPa [37].
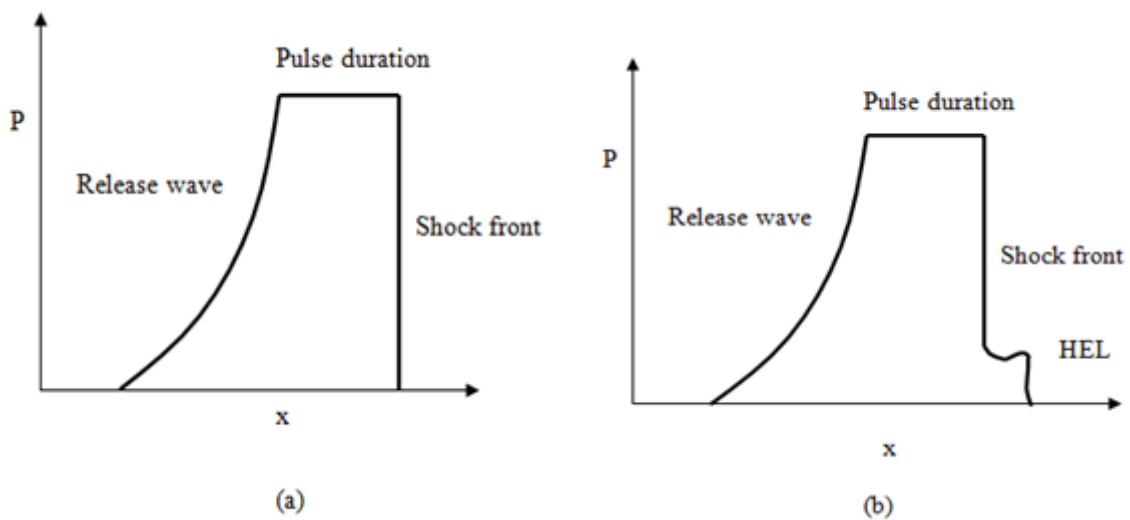
Figure 6: Ideal Shock wave profile (Left), Real wave profile in solids (Right)

Stress analysis of the state of stress under shock loading condition is essential to comprehend the deformation process under extreme conditions. The state of stress in a planar shock wave involves uniaxial strain compression. Suppose that the material is compressed uniaxially in the z-direction, then $\varepsilon_{zz} \neq 0$ and all other stain components are zero. If no plastic deformation (no dislocations) is involved in the wave propagation, linear elasticity theory predicts the following relations in equations (1) and (2):

$$\sigma_{xx} = \sigma_{yy} = \frac{\upsilon}{1 - \upsilon}\sigma_{zz} \tag{1}$$

$$\tau = \frac{1}{2}\left(\sigma_{zz} - \sigma_{yy}\right) \tag{2}$$

Where υ is Poisson's ratio and τ is the maximum shear stress at the wave front. In the shock wave loading of solids, the longitudinal component of the stress is defined as the pressure $(P = -\sigma_{zz})$ since it is the driving force of the shock wave, in fluids however the pressure is equal to the hydrostatic pressure. When the applied pressure exceeds the HEL, the material deforms plastically. Plastic deformation is mainly produced by a microscopic mechanism controlled by the activities of dislocations. Dislocation activities are the fundamental mechanism for relieving strain in crystalline materials, hence it is expected that the dislocation activities will cause the stresses to have different values than those given by the elasticity theory.

D. Scope of Thesis

It is obvious that magnesium single crystal research requires more investigation on both experimental and simulation aspects. Fundamental deformation mechanisms in Mg are subject to discussion, as prior work has often been controversial or inconclusive. The overall objective of this work is to study the slip deformation mechanism in HCP metals with the focus on magnesium using a computational approach. The organization of the thesis is as follows:

- The current understanding of Mg was presented in Chapter I. The crystallographic information, well established mechanical properties, and a review of the current understanding of the deformation mechanisms is given.

- The methodology of the current study is presented in Chapter II. A description of the used Multi-Scale Dislocation Dynamic Plasticity (MDDP) code with the modifications, along with simulation setups is shown.

- In Chapter III, a detailed investigation of the effect of the following parameters on the yield stress, strain hardening and microstructural evolution is carried out.
    - Effect of orientation-dependent dislocation mobility and Peierl's Stress.
    - Size Effect: Simulation results are presented for bulk crystal and for a finite one, with their effect on yield stress and hardening rate.
    - High Strain Rate Loading
    - Shock Loading
    - Effect of crystal orientation: Two main orientations are studied here that corresponds to pyramidal and basal slip

- Chapter IV gives concluding remarks and perspectives for future work.

Chapter II

METHODOLOGY

A. Multi-Scale Dislocation Dynamic Plasticity (MDDP)

MDDP is hybrid elasto-viscoplastic simulation model coupling discrete DD with finite element (FE) analysis developed by Prof. H. Zbib and collaborators. DD is used to determine plastic deformation in single crystals by the evaluation of the dislocation evolution history. Dislocation lines and curves are represented by discrete straight segments of leading and trailing partials bonded by a stacking fault. At each time step, the Peach-Koehler (PK) force is calculated at each dislocation segment by accounting for the dislocation interactions among each other, the dislocation interactions with other defects and obstacles, the image force from the boundary, the Peierl's force, the stacking fault bonding, and the externally applied load. For a dislocation segment, PK force can be expressed as:

$$F_s = F_{Peierls} + F_D + F_{Self} + F_{SF} + F_{External} + F_{Obstacle} + F_{image} \tag{3}$$

The dynamic dislocations is governed by a "Newtonian" equation of motion, consisting of an inertia term, damping term, and driving force arising from short-range and long-range interactions where the glide velocity 'v' is calculated such that;

$$m_s \dot{v} + \frac{1}{M_s(T,p)} v = F_s \tag{4}$$

In the above equations, 'm_s' is the effective dislocation segment mass, 'M_s' is the dislocation mobility which could depend both on the temperature 'T' and the pressure 'p'. As implied by equation (3), the glide force vector 'F_s' per unit length arises from a variety of sources: Peierl's stress ($F_{Peierls}$), dislocation-dislocation interaction (F_D), self-force (F_{self}), interaction with obstacles ($F_{obstacle}$), image forces (F_{image}). The equation of motion is solved to

find the velocities and thus the plastic strain rate $\dot{\varepsilon}_p$ and the plastic spin W_p are evaluated respectively:

$$\dot{\varepsilon}_p = \sum_{i=1}^{N} \frac{l_i v_{gi}}{2V} (n_i \otimes b_i + b_i \otimes n_i) \tag{5}$$

$$W_p = \sum_{i=1}^{N} \frac{l_i v_{gi}}{2V} (n_i \otimes b_i - b_i \otimes n_i) \tag{6}$$

Where 'l_i' is the dislocation segment length, 'n_i' is a unit normal to the slip plane, 'v_{gi}' is the magnitude of the glide velocity of the segment, 'b_i' is the Burgers vector and 'V' is the volume of the representative volume. The above relations provide the most rigorous connection between the dislocation motion (the fundamental mechanism of plastic deformation in crystalline materials) and the macroscopic plastic strain, with its dependence on strength and applied stress being explicitly embedded in the calculation of the velocity of each dislocation.

In the macro level, it is assumed that the material obeys the basic laws of continuum mechanics, i.e. linear momentum balance and energy balance:

$$div\ S = \rho \dot{v}_P \tag{7}$$

$$\rho C_v \dot{T} = k \nabla^2 T + S \dot{\varepsilon}_p \tag{8}$$

In the above equations, S is the stress, T is the temperature, v_p is the particle velocity, ρ, C_v and K are mass density, specific heat and thermal conductivity respectively. For elasto-viscoplastic behavior, the strain rate tensor $\dot{\varepsilon}$ is decomposed into an elastic part $\dot{\varepsilon}_e$ and plastic part $\dot{\varepsilon}_p$ such that:

$$\dot{\varepsilon} = \dot{\varepsilon}_e + \dot{\varepsilon}_p \tag{9}$$

For most metals, the elastic response is linear and can be expressed using the incremental form of Hooke's law such that:

$$S = [C^e]\dot{\varepsilon}_p \tag{10}$$

Where C^e is in general the anisotropic elastic stiffness tensor for cubic symmetry.

Combining (9) and (10) leads to:

$$S = [C^e][\dot{\varepsilon} - \dot{\varepsilon}_p] \tag{11}$$

Details of this model are described elsewhere [38, 39, 40].

.

B. Incorporation of HCP Crystallography in MDDP

MDDP framework was originally developed for FCC and BCC materials. In our work here, the framework is modified to accommodate for HCP materials. The commonly used frame of reference to describe slip planes and directions in HCP materials is the hexagonal system. In such system, a slip direction will have 4 coordinates; this notation is called Miller-Bravias. The four-axis system is based on the a_1, a_2, a_3 and c vectors as shown in figure 7 below.
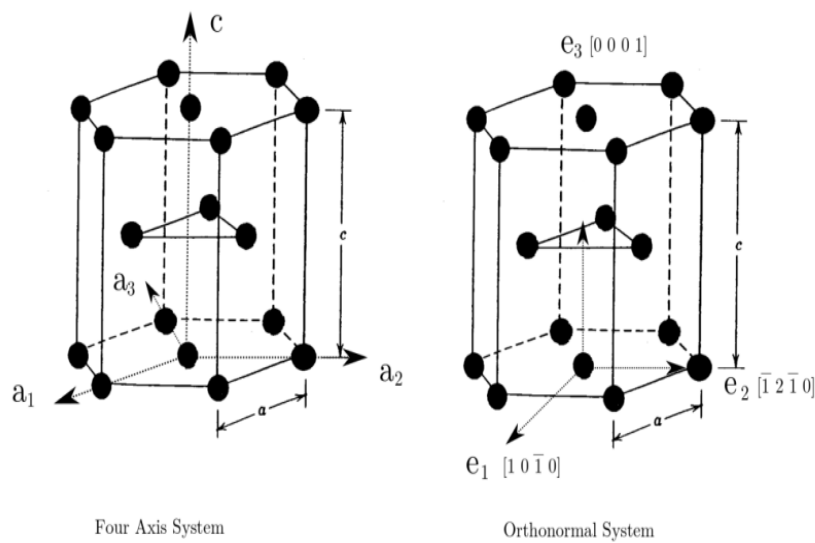
Figure 7: Four-axis system (Left), three-axis orthonormal system (Right)

19

As mentioned earlier, dislocation glide in HCP metals may occur on the basal, prismatic, or pyramidal planes depending on the resolved shear stress on these planes and the their corresponding frictional stresses. Since the MDDP code operates with three-axis orthonormal coordinate system, slip planes and Burgers vectors are transformed from four-axis Miller-Bravias notation to three-axis orthonormal coordinate system such that unit vector magnitude is equal to a (lattice length). In symmetric crystal structures, slip planes are defined by their respective normal vector having the same indices. However, in Miller-Bravias indices, a direction is not always normal to a plane of the same indices. The transformation from the four-axis plane (hkil) to the normal direction [a_1 a_2 a_3 c] can be expressed as below in equation (12) [4].

$$[a_1\ a_2\ a_3\ c] = \left[h\ k\ i\ \left(1.5 \times \left(\frac{a}{c}\right)^2 \right) l \right] \tag{12}$$

Table 3: Transformation of slip planes (4-axis indices) to normal vector (3-axis indices)

Slip Plane Type	4-axis Plane (hkil)	Normal Vector [a_1 a_2 a_3 c]	3-axis [x y z]
Basal	(0 0 0 1)	[0 0 0 1]	[0 0 1]
Prism 1	(1 0 $\bar{1}$ 0)	[1 0 $\bar{1}$ 0]	[1 0 0]
Pyramidal 1	(1 0 $\bar{1}$ 1)	[1 0 $\bar{1}$ 0.56]	[1.73 0 0.92]
Pyramidal 2	(1 1 $\bar{2}$ 2)	[1 1 $\bar{2}$ 1.12]	[0.866 0.5 0.61]

C. Schmid Factor Calculation

The calculation of the schmid factor is important to identify the activity of different slip planes for various loading directions. However, it is not well known in HCP materials, as the asymmetry of the crystal, c/a ratio and the 4-indices Miller-Bravias coordinates make it more complicated that FCC materials. To obtain the schmid factor, it is necessary to calculate that dot product between the loading direction **L: [u₁ v₁ t₁ w₁]** and slip direction **S: [u₂ v₂ t₂ w₂]**, as well as perpendicular direction **R: [u v t w]** to plane p: (h k i l). A generalized form for calculation of the **schmid factor (SF)** in HCP materials is as below:

$$SF = \cos(L.S) \times \cos(L.R) \tag{13}$$

$$\cos(L.S) = \frac{L.S}{|L||S|} = \frac{u_1u_2 + v_1v_2 + t_1t_2 + \alpha^2w_1w_2}{\sqrt{(u_1^2 + v_1^2 + t_1^2 + \alpha^2w_1^2)} \cdot \sqrt{(u_2^2 + v_2^2 + t_2^2 + \alpha^2w_2^2)}} \tag{14}$$

With,

$$L.S = \frac{3a^2}{2}(u_1u_2 + v_1v_2 + t_1t_2 + \alpha^2w_1w_2) \tag{15}$$

$$\alpha^2 = \frac{2}{3}\left(\frac{c}{a}\right)^2 \tag{16}$$

If R: [u v t w] is the normal vector to a plane p: (h k i l), they are related by:

$$[u\ v\ t\ w] = [h\ k\ i\ l(\alpha^{-2})] \tag{17}$$

$$\cos(L.R) = \frac{L.R}{|L||R|} = \frac{u_1h + v_1k + t_1i + w_1l}{\sqrt{(u_1^2 + v_1^2 + t_1^2 + \alpha^2w_1^2)} \cdot \sqrt{(h^2 + k^2 + i^2 + \alpha^{-2}l^2)}} \tag{18}$$

$$SF = \frac{u_1u_2 + v_1v_2 + t_1t_2 + \alpha^2 w_1w_2}{\sqrt{(u_1{}^2 + v_1{}^2 + t_1{}^2 + \alpha^2 w_1{}^2)} \cdot \sqrt{(u_2{}^2 + v_2{}^2 + t_2{}^2 + \alpha^2 w_2{}^2)}}$$
$$\times \frac{u_1h + v_1k + t_1i + w_1l}{\sqrt{(u_1{}^2 + v_1{}^2 + t_1{}^2 + \alpha^2 w_1{}^2)} \cdot \sqrt{(h^2 + k^2 + i^2 + \alpha^{-2}l^2)}} \tag{19}$$

Table 4 provides a summary of the schmid factor calculation for the slip planes for common loading directions. The [0 0 0 1] orientation provides a non-zero schmid factor only for pyramidal II planes. A-axis loading of orientation [10$\bar{1}$0], [11$\bar{2}$0] gives a zero schmid factor for basal slip, with the prismatic slip system having the highest value.

Table 4: Schmid factor calculation for common slip planes and loading directions

Loading Direction / Slip System	[0 0 0 1]	[11$\bar{2}$0]	[10$\bar{1}$0]	[10$\bar{1}$1]	[2$\bar{1}$$\bar{1}$2]
Basal	0	0	0	**0.43**	**0.5**
Prismatic I	0	**0.43**	**0.43**	0.23	0.2
Pyramidal I	0	0.38	0.38	0.41	0.29
Pyramidal II	**0.45**	0.44	0.33	0.22	0.3

D. Simulation Setup

Figure 8: Sample simulation setup for (a) uniaxial loading and (b) shock loading

The simulation setup (see Figure 8a) is deigned to mimic the uniaxial compression experiment of magnesium single crystals oriented for basal and non-basal orientations. The base simulation domain has a squared cross-sectional area with an aspect ratio of two; the dimensions are taken as 5 μm × 5 μm × 10 μm. To achieve the uniaxial compression loading, a velocity-controlled boundary condition is applied on the upper surface so that a constant strain rate loading is attained. The bottom surface is rigidly fixed while the four sides are kept free. Initially, Frank-Read sources, with lengths that range between 1.2 μm to 2 μm, are used

23

as agent for dislocation generation. The dislocation sources are randomly distributed on slip planes with a dislocation density of about 1.2×10^{12} m^{-2}. In dislocation dynamics (DD), periodic boundary condition is used to model dislocation motion in bulk crystals in a way that when a dislocation reaches one end of the simulation domain it comes back from the other end. In contrast, simulation of finite crystal has a free boundary condition in DD such that when a dislocation reaches the end of simulation domain, it is absorbed. To simulate pyramidal slip, the crystal is loaded in the [0 0 0 1] direction that correspond to the z-axis. However, to simulate basal slip, the crystal is loaded in the [$2\bar{1}\bar{1}2$] which corresponds to the 45 degrees orientation. Thus, the crystal is oriented 45 degrees, such that the z-axis coincides with the loading axis now. The simulation setup and a sketch for the crystal orientation correspondent to the above cases are shown in Table 5 and figure 9 respectively. In Table 6, the Peierl's stress of the slip planes is displayed. Also, because of the anisotropy in HCP crystals, all simulated samples are set to have anisotropic elasticity as per Table 7.

Table 5: simulation setup for different orientations

Slip System	Pyramidal Slip	Basal Slip
Crystal Orientation	[0 0 0 1]	[$2\bar{1}\bar{1}2$]
Simulation Domain (μm)	$5 \times 5 \times 10$	$5 \times 5 \times 10$
Initial Dislocation Density (m^{-2})	1.2×10^{12}	2.9×10^{12}
Strain rate (s^{-1})	10^3	10^3

Figure 9: Crystal orientation for (a) pyramidal slip (b) basal slip

Table 6: Peierl's Stress for the slip systems

Slip System	Peierl's Stress (MPa)	Reference
Basal	0.5	Burke et al. [5] Yoshinaga et al. [10]
Prismatic	39.2	Reed-Hill and Robertson [14]
Pyramidal	105	Staroselsky and Anand [41]

Table 7: Elastic anisotropy in magnesium [42]

Elastic Constant	Value (GPa)
C_{11}	59.7
C_{33}	61.7
C_{44}	16.39
C_{12}	26.2
C_{13}	21.7

As the literature lacks data regarding the values of dislocation mobility, a parametric study for dislocation mobility helps unveil some of important characteristics of dislocations:

Table 8 shows cases that correspond to the c-axis compression of a 5 x 5 x 10 μm simulation volume with different dislocation mobility ranging between 10^2 to 10^5 $(Pa.s)^{-1}$.

Table 8: Four Cases with different mobility values

Case	Dislocation Mobility $(Pa.s)^{-1}$
1	100,000
2	10,000
3	1000
4	100

As it is known that edge dislocations possess higher mobility than screw ones in dislocations of type <c+a> acting on pyramidal planes, the effect of the ratio of edge over screw dislocation mobility is investigated: Table 9 shows the four cases, studied here, with ratios between 1 and up to 10^3 where a ratio of one corresponds to same dislocation mobility for all dislocation character.

Table 9: Case 1-4 for different edge over screw dislocation mobility ratio

Case	Edge Dislocation Mobility $(Pa.s)^{-1}$	Screw Dislocation Mobility $(Pa.s)^{-1}$	Edge / Screw Dislocation Mobility Ratio $(Pa.s)^{-1}$
1	100,000	100,000	1
2	100,000	10,000	10
3	100,000	1,000	100
4	100,000	100	1,000

Regarding size effect, the studied cases are summarized in Table 10 below. All simulation domains are set to have a squared-cross sectional area with a constant aspect ratio of two. Also, a constant strain rate of $(10^3 \ s^{-1})$ is maintained with varying FR source lengths depending on domain length, such that FR sources lengths are less than half the length of the

simulation domain. All cases possess a close initial dislocation density in the range of 2.5 - 3 $\times 10^{12}$ (m^{-2}).

Table 10: Summarized simulation setup for size effect

Simulation Domain (µm)	$0.5 \times 0.5 \times 1$	$0.9 \times 0.9 \times 1.8$	$1.2 \times 1.2 \times 2.4$	$1.8 \times 1.8 \times 3.6$	$3 \times 3 \times 6$	$5 \times 5 \times 10$	$6 \times 6 \times 12$	$8 \times 8 \times 16$	$10 \times 10 \times 20$
FR Sources Length (µm)	0.2-0.25	0.3 - 0.4	0.5-0.6	1 - 1.2	1.2 - 1.5	**1.5 - 2**	2 - 2.5	3 – 3.5	4 - 4.5
Initial Dislocation Density (m^{-2})	2.8×10^{12}	2.6×10^{12}	2.7×10^{12}	2.8×10^{12}	3×10^{12}	$\mathbf{2.7 \times 10^{12}}$	2.8×10^{12}	2.5×10^{12}	2.6×10^{12}

For investigation of the strain rate effect on the yield stress and the hardening rate, the following simulation setup is shown below in Table 11 with same sample size and varying the strain rate.

Table 11: Simulation setup for strain rate effect

Simulation Domain (µm)	$\mathbf{5 \times 5 \times 10}$
Initial Dislocation Density (m^{-2})	2.8×10^{11}
Strain rate (s^{-1})	10^2 - 10^7

The lower crystal symmetry in HCP materials results in a complex deformation response during shock loading. Figure 8 (b) depicts the simulation domain for the shock loading simulation. Initially, Frank–Read sources are randomly distributed on slip planes of the [0 0 0 1] oriented magnesium single crystals. Periodic boundary condition is used in DD and the simulation domain has dimensions of 1.2 µm × 1.2 µm × 24 µm. Such high aspect

ratio is selected to allow us to observe plasticity during shock loading. Plane shock loading involves uniaxial strain compression, which leads to the propagation of a large-amplitude three-dimensional state of stress in the material. To achieve this loading condition, a velocity-controlled boundary condition is applied on the upper surface such that the velocity increases linearly to its maximum value over a finite rise time period. The velocity is then held constant for a period equal to the shock-holding time. The bottom surface of the computational domain is rigidly fixed with the four sides confined.

Chapter III

RESULTS AND DISCUSSION

A. Pyramidal Slip

1. Bulk Crystal

Two simulation cases are presented below in Table 12, where we introduced mobility based on dislocation character. Case A has constant mobility values for all dislocations and is taken as base case for comparison. Case B has a very high mobility for edge dislocations, and low mobility for screw ones. Mixed dislocation's mobility is taken as a linear function between edge and screw depending on their orientation.

Table 12: Dislocation character mobility for Cases A and B

Cases	Edge Mobility $(Pa.s)^{-1}$	Screw Mobility $(Pa.s)^{-1}$
A	10^5	10^5
B	10^5	10^{-5}

Figure 10 depicts the resulting stress-strain diagrams for the two cases A and B. In case A, the behavior is linear elastic up to 0.45% total strain corresponding to 250 MPa. This large value of the yielding stress is a reflection of the very large frictional stress on the pyramidal-$\pi 2$ plane (105 MPa), in addition to the stress required to bow-out the dislocation sources. The behavior then assumes a perfect plasticity behavior from 0.5% to 0.7% with no hardening effect. Case B corresponds to the varying mobility case, and the stress-strain curve shows hardening behavior from 0.6 % to 1%. The small fluctuations in the stress-strain curve correspond to the formation and breakage of dipoles. To the best of the authors' knowledge,

this result is the first DD simulation to show strong hardening as reported in many experiments. It is worth noting that additional simulations of high mobile screw segments and stationary edge segments have been carried out and showed similar behavior as in case A.
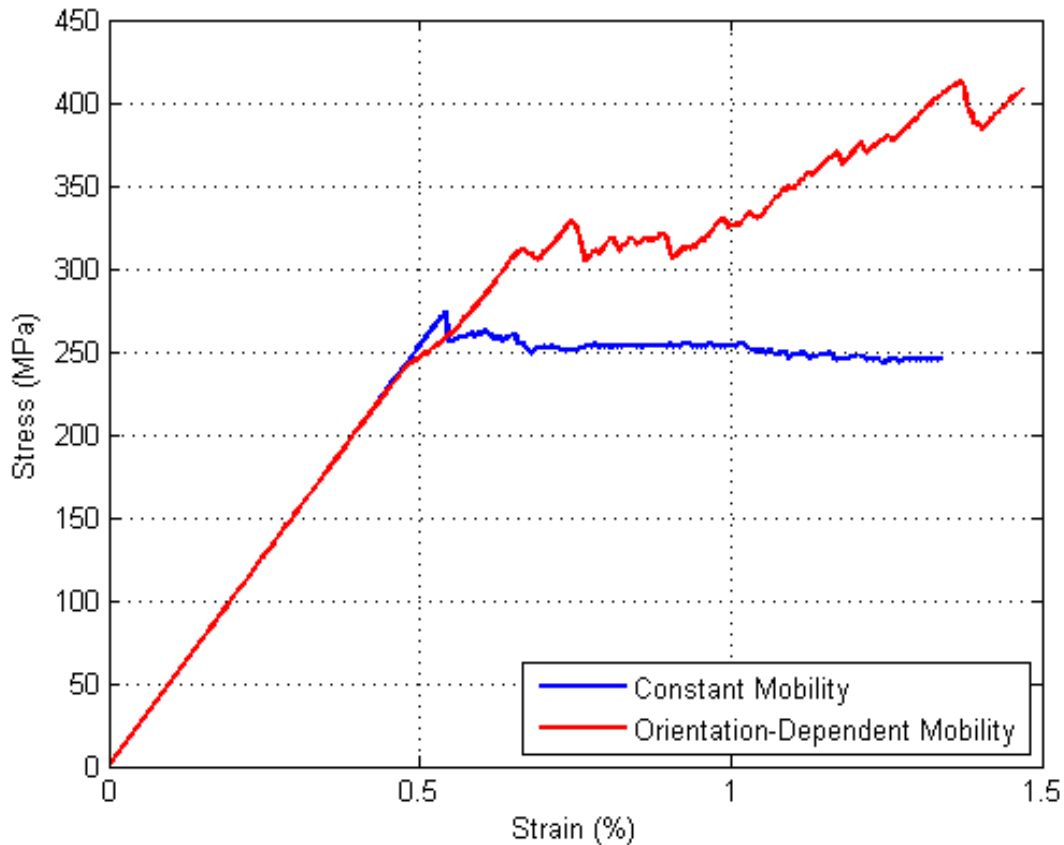

Figure 10: Obtained Stress-Strain Curve for Cases A and B

Figure 11 shows snapshots of the dislocation microstructure evolution for case B. As shown in figure 11(a), numerous dislocation sources are initially placed on the slip planes. As the stress increases, the activation stress for some of the dislocation sources is attained leading to the bow-out of these sources figure 11(b) and to the increase in the dislocation density. It is worth mentioning that sources placed on the pyramidal planes can only be activated due to the fact that in c-axis compression, only pyramidal planes have non-zero Schmid factors (0.45). Additionally, since the screw segments are assumed as nearly stationary, we see that pure edge segments sweeps through the crystal at very high speed

leaving behind extended dipoles of screw type (see figure 11(b), (c)). The process continues

leading to the accumulation of the dislocation slip on the pyramidal planes in the form of slip

bands. Eventually, the simulation domain becomes full of intersecting slip bands with very

high dislocation density formed. A contour view for the variation of the effective plastic

strain is shown in figure 12, where the high strain area corresponds to the pyramidal slip
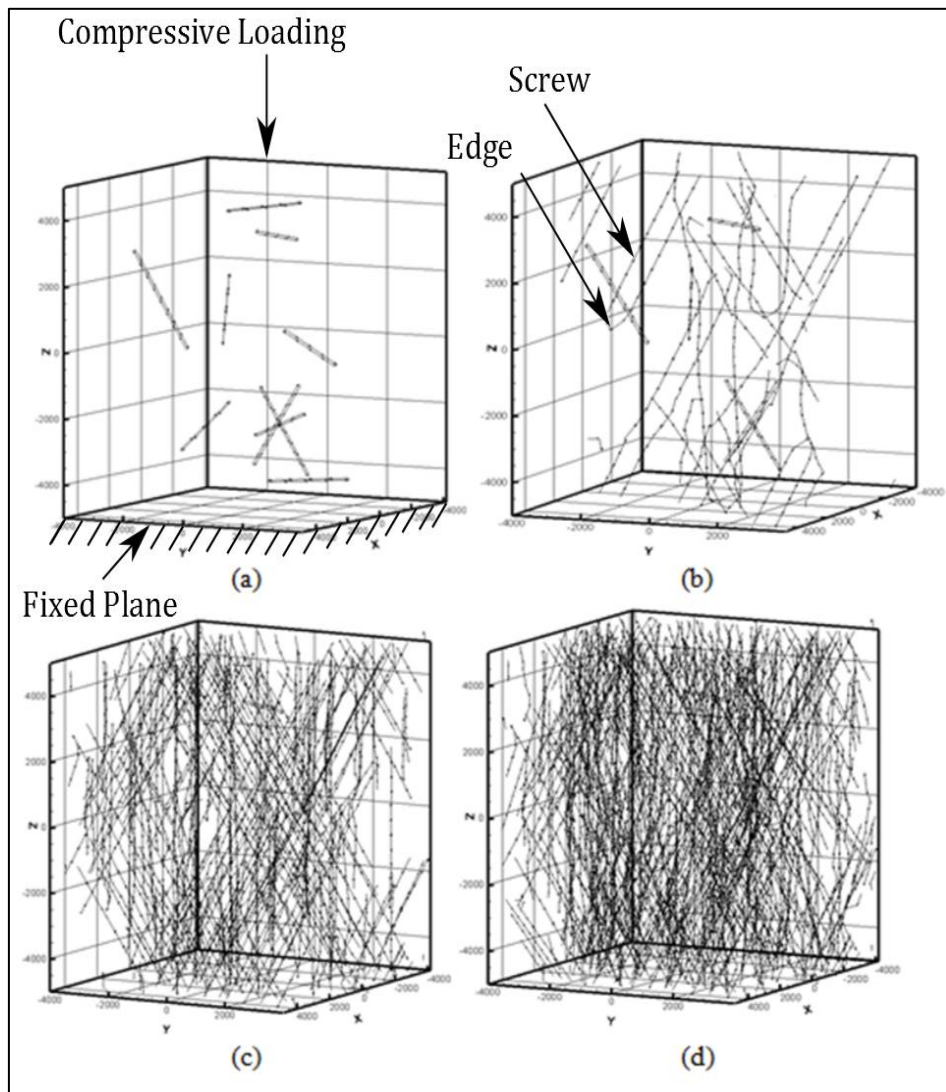
planes.

Figure 11: Snapshots of the microstructure evolution in Simulation B. (a) Initial dislocation sources (b) Activation of dislocation sources on pyramidal plane (c) Dislocation glide and activation of new sources (d) Slip bands with dense dislocations are formed

Figure 13 shows the evolution of the dislocation density versus time for case B. Clearly the curve shows three distinct regimes. The first one corresponds to time when stress is still below the resolved shear stress required to activate the dislocation sources. In that case, dislocations do not move and the dislocation density stays at its initial value of $10^{12}\,\mathrm{m}^{-2}$. As the stress increases, the resolved shear stress reaches the critical value activating the dislocation sources and an abrupt increase in the dislocation density is observed. The process of dislocation emission continues but at a lower rate and eventually dislocation density saturation is attained.
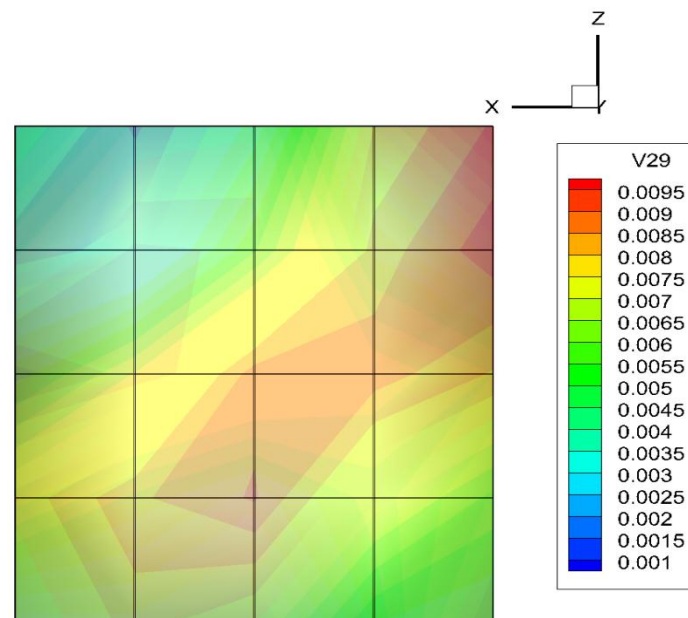

Figure 12: Contour view of the effective plastic strain variation across the simulation volume
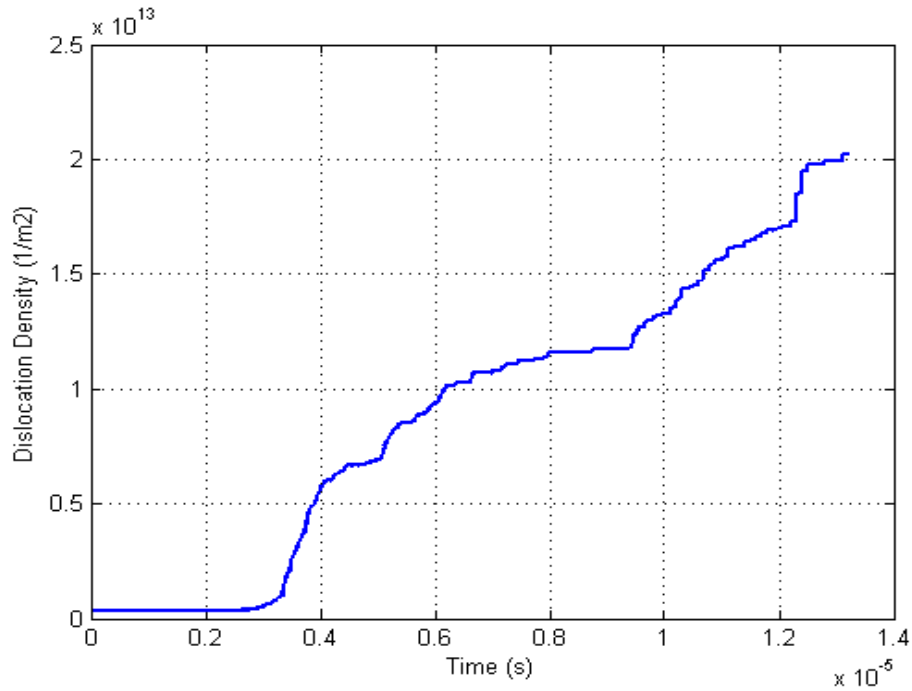
Figure 13: Dislocation Density Increase versus Time

2. Finite Crystal

<u>a. Mobility Study</u>

Figure 14 shows the obtained stress-strain curves for different mobility values as shown in Table 8. It is clear that as mobility decrease, the yield stress goes higher. A decrease in dislocation mobility means that stress must reach a higher state before the activation of the sources. We observe an overall close behavior for cases 1 and 2 regarding yield stress, but with cases 3 and 4 displaying an offset in the stress levels. From the figure, it is suggested that the mobility value must be somewhere between 10^4 and 10^5 Pa.s^{-1} as the corresponding curves begin to overlap and produce a yield stress in the region of 250-300 MPa as reported in the c-axis microcompression experiments for 5 μm [8] [20].
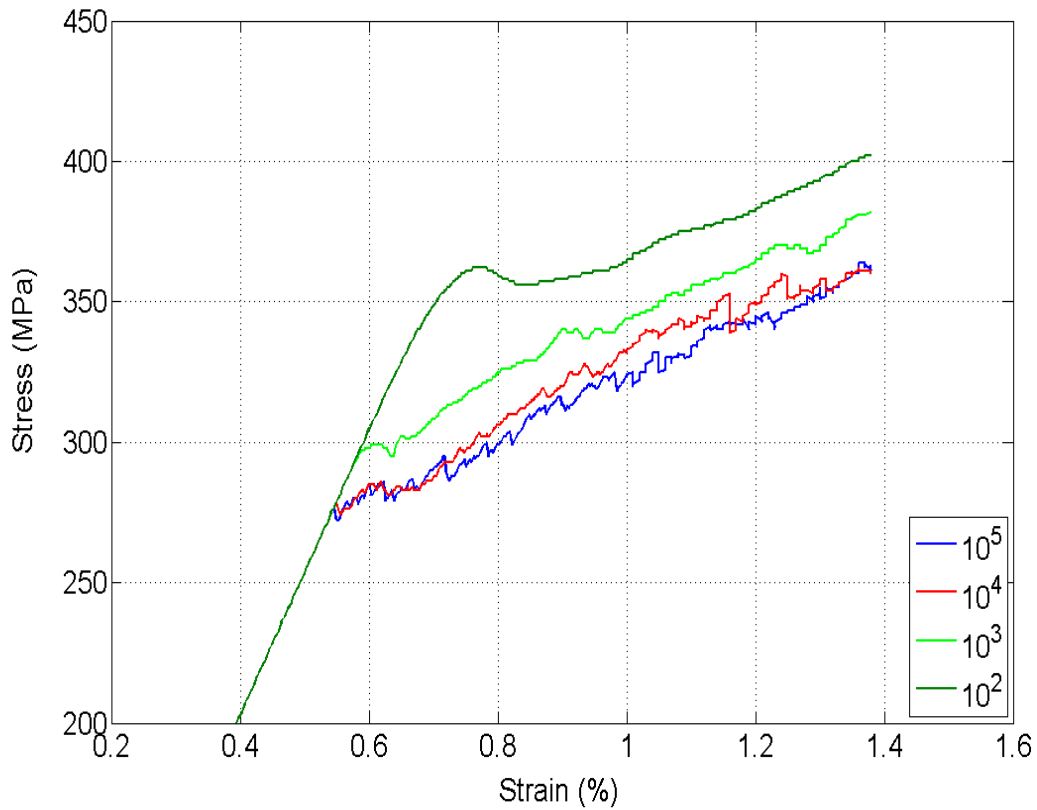
Figure 14: Stress-Strain curves for different mobility values

Figure 15 shows the stress-strain curves for the four cases in table 9: It is clear that as the ratio of mobility increases, the yield stress is increased. This is related to microstructural evolution of dislocations shown in figure 16. One notices that for case 1, dislocations are of different character (edge, screw and mixed). In contrast, most dislocation, that correspond to case 4, are of screw types as edge dislocation glide very fast leaving behind screw ones.
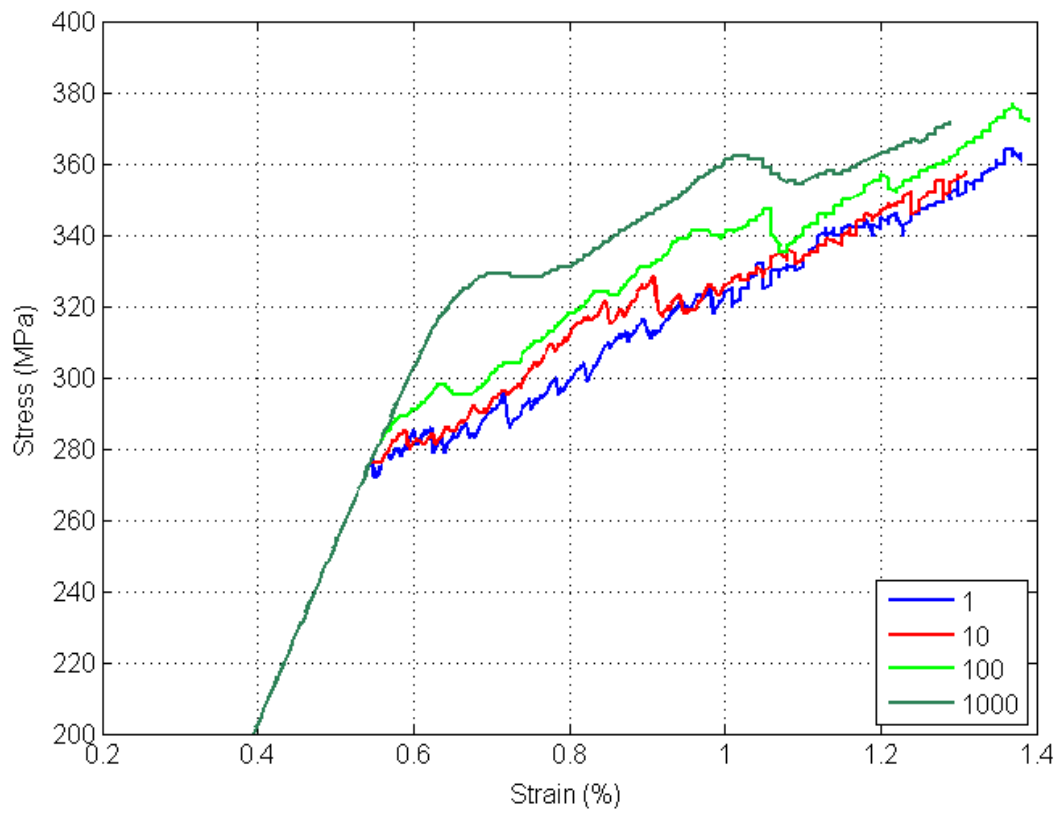
Figure 15: Stress-Strain curves for different ratios of edge over screw dislocation mobility
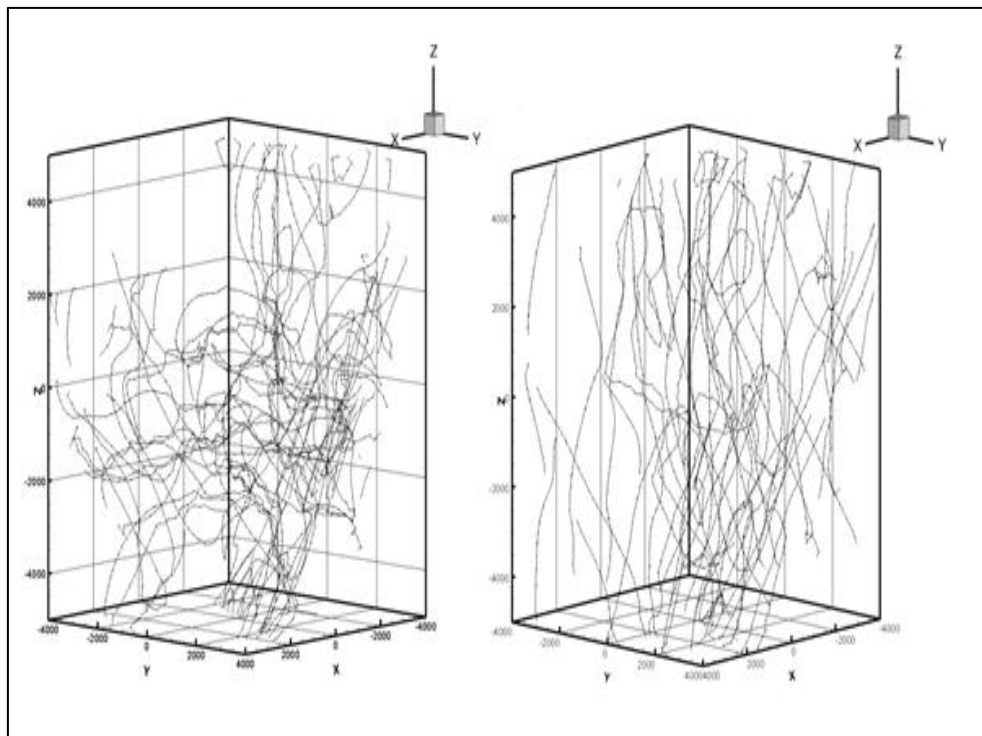

Figure 16: Simulation domains for Case 1 (Left) and Case 4 (Right) as per Table 9

35

Regarding reports for the anisotropy in dislocation-character Peierl's stress [35, 43], many cases have been tested for different combinations of values for dislocation orientation-dependent Peierl's stress. The obtained results didn't show a change in the plasticity behavior in the stress-strain curves. This can be related to the fact that Peierl's stress is the stress required only to initiate motion, which is then controlled by mobility values.

b. Size Effect

New technological developments have required a more comprehensive investigation of the material at a smaller scale. A better understanding of size-effect behavior allows for optimization of Mg properties in such applications. Size effect is usually attributed to the trend that flow stress increases with decreasing specimen size. Recently, the use of new micro-compression experimental technique, by some researchers, has allowed the study of size effect of materials such as: Nickel (Ni) [44], Gold (Au) [45], and Mg [8, 12, 21, 46].

Generally, the above micro-compression tests show size effect on the yield stress and/or the strain hardening with different explanation of the observed behavior. Greer et al. [45] performed micro-compression tests on Au pillars, observing size effect only on the flow stress. They described the observed size effect with the idea of "dislocation starvation", that is, as the specimen size gets smaller, dislocation density goes lower due to dislocations escaping out of the pillar through image forces and thus a higher stress is required to activate new sources and continue plasticity. However, Norfleet et al. reported that dislocation density actually increase with deformation. They explained this by the concept of "weak source": In microcrystals, there exist a fewer number of weak sources compared to bulk ones which bears numerous dislocation sources to accommodate plasticity.

Recently, micro-compression experiments have been applied on pure, single crystalline Mg. As HCP materials show an orientation-dependent behavior, size effect was studied for the two main orientations: basal and pyramidal II slip. For (0001) oriented Mg single crystals, Lilleodeen et al. and Byer et al. [21, 46] observed a size effect only in the flow stress for pillar diameters between 1 μm and 10 μm. In a more recent study, Byer et al. [46] investigated the effect of initial dislocation density on the size effect for both orientations. It was concluded that samples having high initial dislocation density show little or no size effect, while those of low initial dislocation density display a size effect on the flow strength and strain hardening rate. This behavior was explained such that increasing the initial dislocation density means having a larger number of weaker sources, and the "weak source" mechanism is stopped. Regarding the influence of the crystal orientation on size effect, the effect of crystal anisotropy on the plastic flow was clear, as basal-slip-oriented crystals display a stronger size effect than pyramidal II ones. A similar observation was made by Kim [8], who attributed this difference to the multiple slip behavior (six pyramidal slip planes) compared to single slip (one basal plane).

Figure 17 below shows the compressive yield strength as a function of sample length for c-axis compression orientation. The simulated samples have a squared cross-section and an aspect ratio of two. The displayed yield stresses are as per the 0.2 % strain criteria as predicted by 3DDD Simulations. In addition, experimental results on c-axis compression on pure Mg by Byer et al. [46], Kim [8], and on Mg AZ31 alloy by Aitken et al. [12] are shown here for comparison.
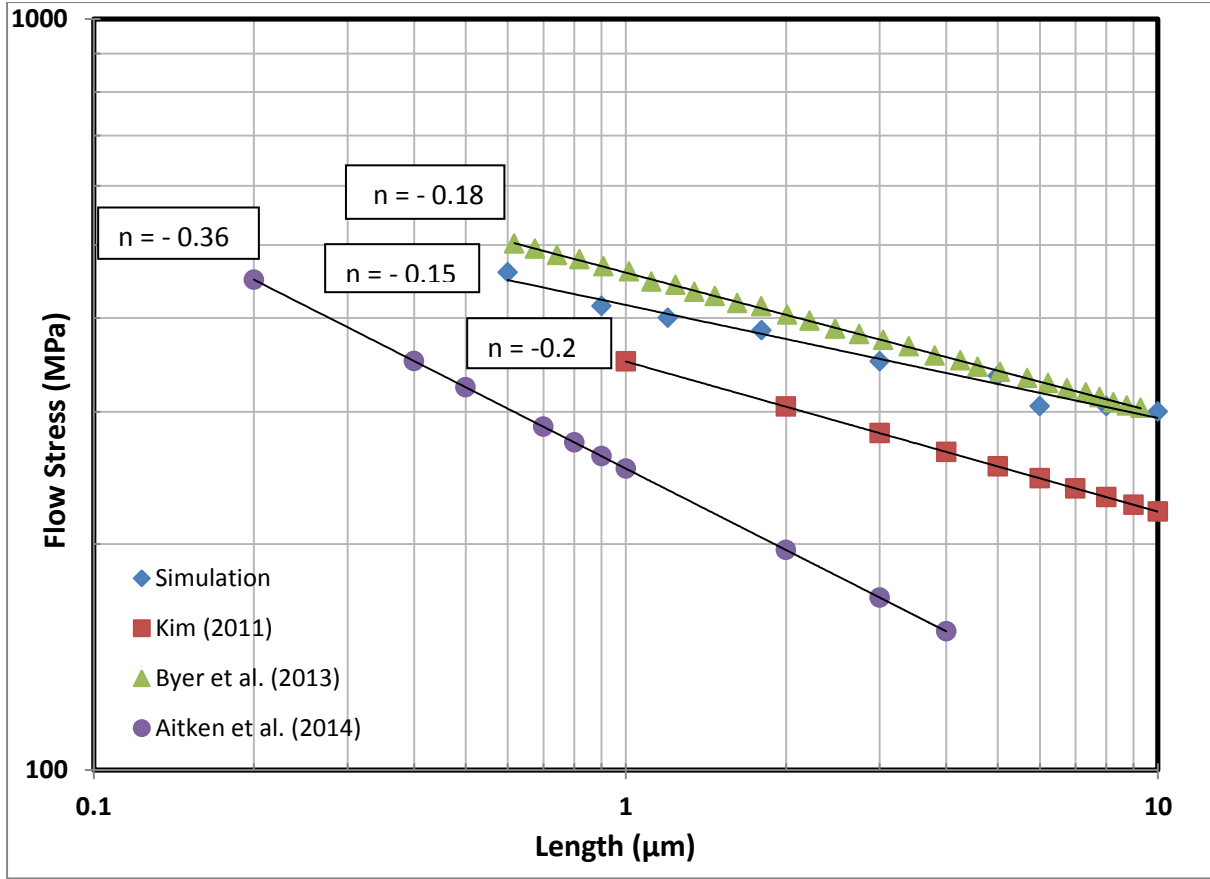
Figure 17: Log-log plot of the variation of flow stress (MPa) with size (μm)

All curves show a clear power law of form ($\tau \propto 1/D^n$), each with a best fit power exponent n. The predicted power law exponent n = - 0.15, by our simulations, is close to that of Byer et al. [46] (n= - 0.18) and kim [8] (n= - 0.2). The slight difference in exponents from Aitken et al. [12] (n=-0.36) can be attributed to the size range of 0.2 to 5 μm from Aitken [12] data as compared to the remaining data ranges of 1 to 10 μm. Variation in stresses is related to the % strain at which flow stress is taken. Another variation might be related to the different initial microstructure and dislocation density of the tested samples. The stress required for dislocation sources movement and multiplication is described as below:

$$\tau = \frac{\alpha \times G \times b}{L} \qquad (20)$$

Where τ is the required resolved shear stress to bow out the dislocation, α = 0.5-1, G is the shear modulus, b is the Burgers vector length, and L is the length of the Frank-Read source.

As the dislocation source length gets smaller, more stress is required for the source to bow out.

Figure 18 shows the stress-strain curves for only two samples lengths for simplicity. An important observation here is the serration in the stress-strain curves; That is, as the size gets smaller, the serration in the curves gets larger. Figure 19 shows the microstructure of two sample lengths: 0.5 μm to the left and 3 μm to the right at 2% total strain. It is clear that the small sample contains fewer dislocations, and eventually this small number of dislocations will affect plasticity such that small burst displacement appears as serration. This behavior was also observed by kim [8] and Lilleodden et al. [21].
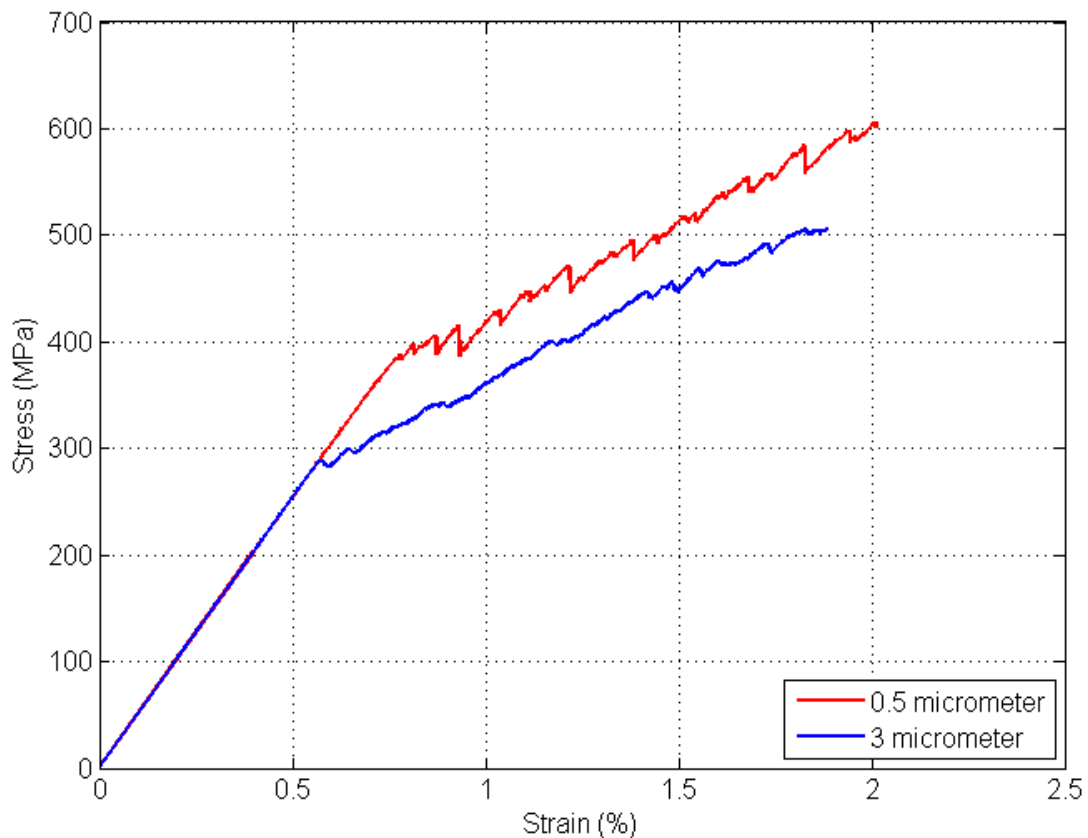

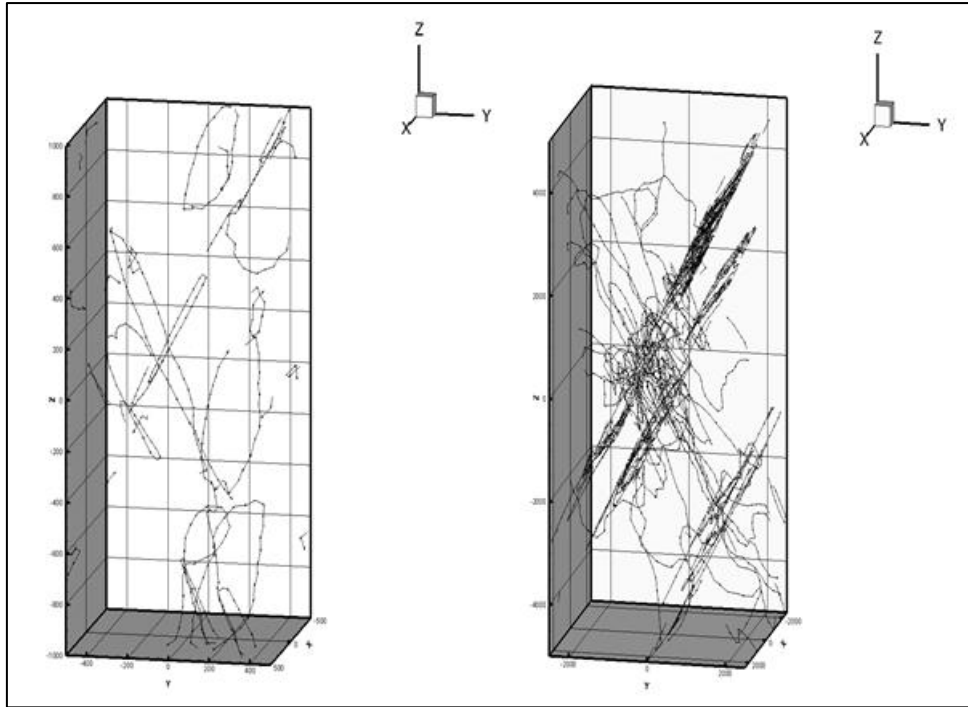Figure 18: Stress-Strain curves for two sample sizes

Figure 19: Microstructure for two sample lengths 0.5 μm (Left) and 3 μm (Right)

It is obvious that the flow stress is size dependent, now the hardening rate variation for different simulation sample sizes is investigated. Figure 20 provides a log-log plot for the variation of the hardening rate with size for our simulation and for experimental results by Kim [8] and Byer et al. [46]. The obtained best fit power exponent for our simulations (n = -0.09) is close to the experiments (n= - 0.12 and n= - 0.10). However, the discrepancy between the hardening rates of experiments and the predicted simulation values is related to range of strain over which the average hardening rate is calculated. Because of computational limitations, we can simulate up to 1.5 – 2 % strain at a strain rate of 10^3 s^{-1} compared to experiments that go up to a strain of 10 %.
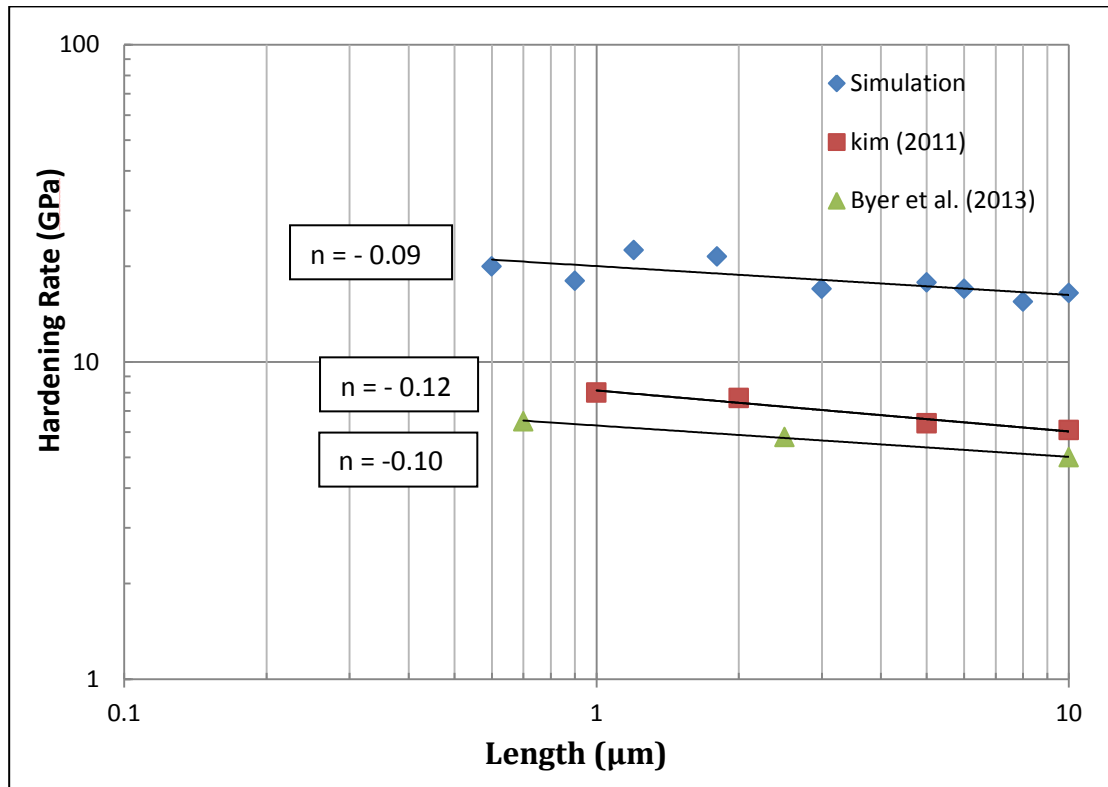
Figure 20: Log-log plot of the Variation of Hardening Rate (GPa) with Size (μm)

c. Strain rate effect:

It is known that the applied strain rate significantly affect the deformation mechanisms. Examples of high strain rate conditions are those generated in high speed machining, ballistic impact, explosive welding, armor protection, vehicle crash testing and so forth. High strain rate loading of Mg alloys has been the focus of the majority of prior studies. A study by Prasad et al. [47] revealed that strain rate sensitivity is dependent on the deformation mechanisms: When deformation is governed by twinning, materials show rate-insensitive strengths in contrast to deformation by slip which shows rate dependence of the flow stress. In addition, Tucker et al. [48] performed high strain rate tests on rolled Mg AZ31 alloy and revealed strong strain rate dependence on the compressive yield, hardening rate and ductility in the normal direction. However, samples loaded in the transverse and rolling directions didn't show any strain rate dependence. High strain rate loading of pure Mg was

41

also investigated by Dixit et al. [49]: The observed high strain hardening rate was associated with dislocation activity in the increase in the <c+a> dislocation density and dislocation-dislocation interactions. Magnesium single crystals were tested under ambient compressive loading at a dynamic strain rate of 1000 s^{-1} [16]. The samples were loaded using a Split-Hopkinson Pressure Bar (SHPB) system and had its [0 0 0 1] direction about 10 degrees away from the vertical axis. The microstructure analysis showed activation of prismatic 1 {10$\bar{1}$0} <11$\bar{2}$0> and Pyramidal 2 {11$\bar{2}$2} <11$\bar{2}$3> slip systems. The absence of twinning was related to the faster increase of the critical resolved shear stress (CRSS) of twinning than that of dislocation slip under dynamic loading. The strain stress curve showed strong hardening behavior with a non-distinct transition from elastic to plastic deformation. Besides, the dynamic maximum strength and strain hardening rate were about 30% and 20% higher than the corresponding quasi-static values. This was attributed to the increase in CRSS for slip and twinning as the strain rate increases.

Figures 21 and 22 show the stress-strain curves for strain rates from 10^2 to 10^7. The yield stresses from figures 21 and 22 is plotted versus strain rate on a log-log plot in figure 23. Simulation 1 corresponds to the lower strain rate range of 10^2 to 10^4 while simulation 2 is for the higher strain rate range of 10^4 to 10^7. On the same plot, experimental data for high strain rate loading, at ambient temperature, by Swegle & Grady [50] for Beryllium (Be), Magnesium Oxide (MgO) and Copper (Cu) are shown for comparison. Our predicted simulation power law (n = + 0.27) is in agreements with the experimental one fourth power law (+ 0.25). With the increase in strain rate, the velocity for the displacement increases, leading to an increase in the yield stress. It is noted here that no data exists for the variation of the yield stress versus strain rate for pure Mg.
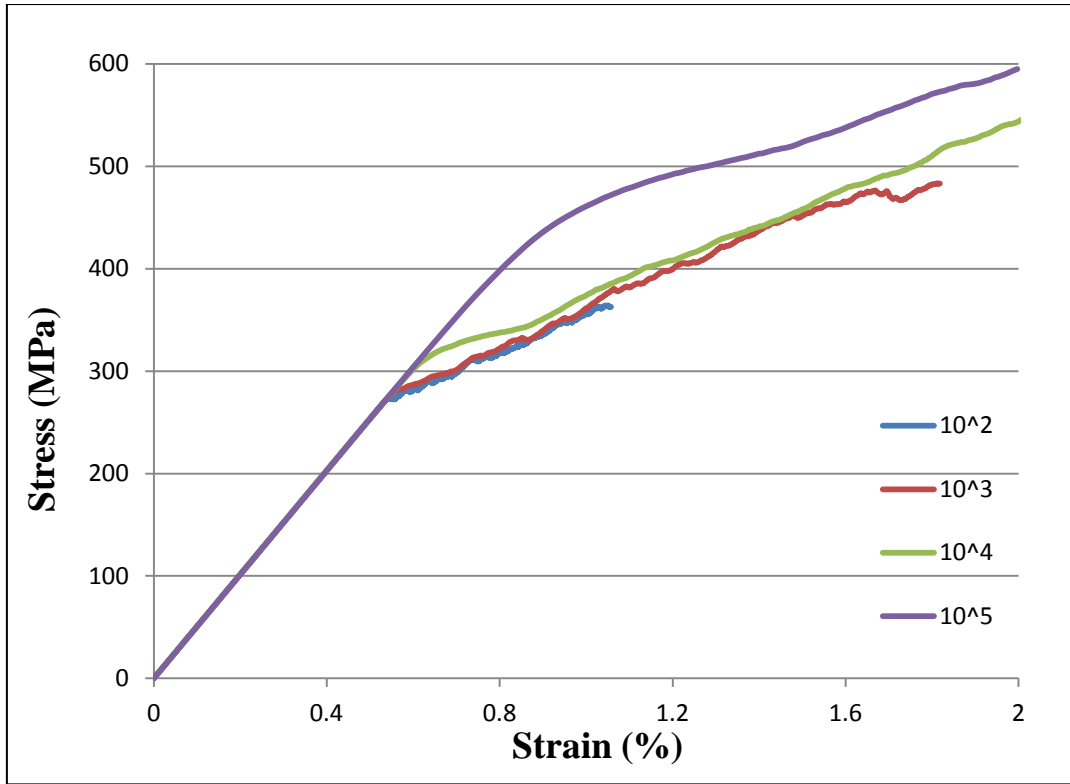
Figure 21: Stress-Strain Curves for strain rates from 10^2 to 10^5
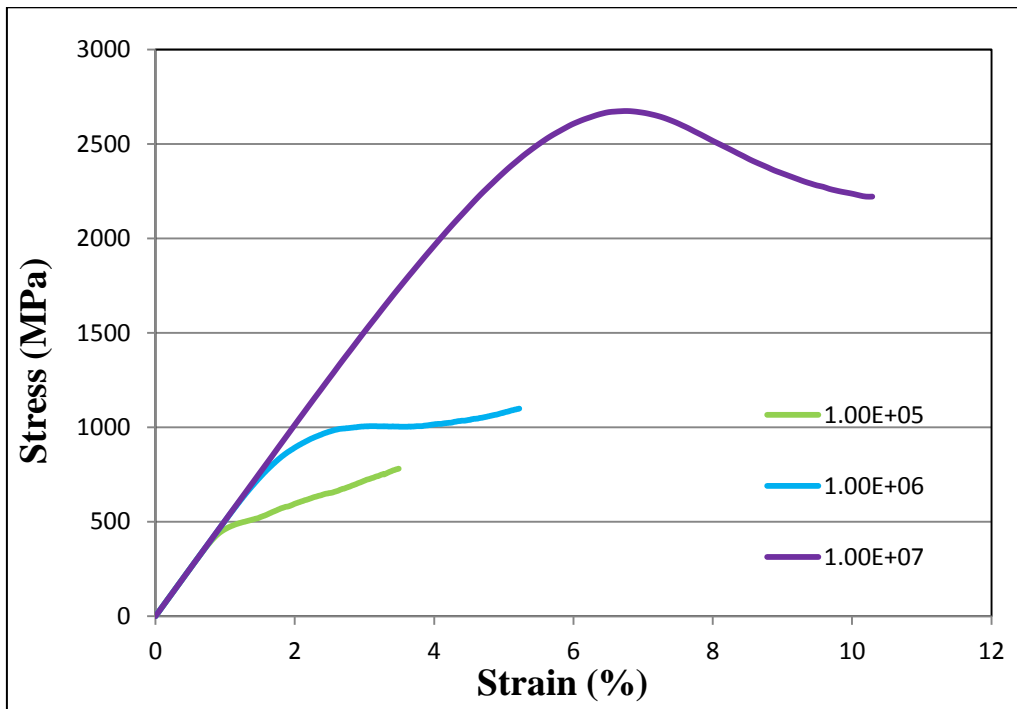

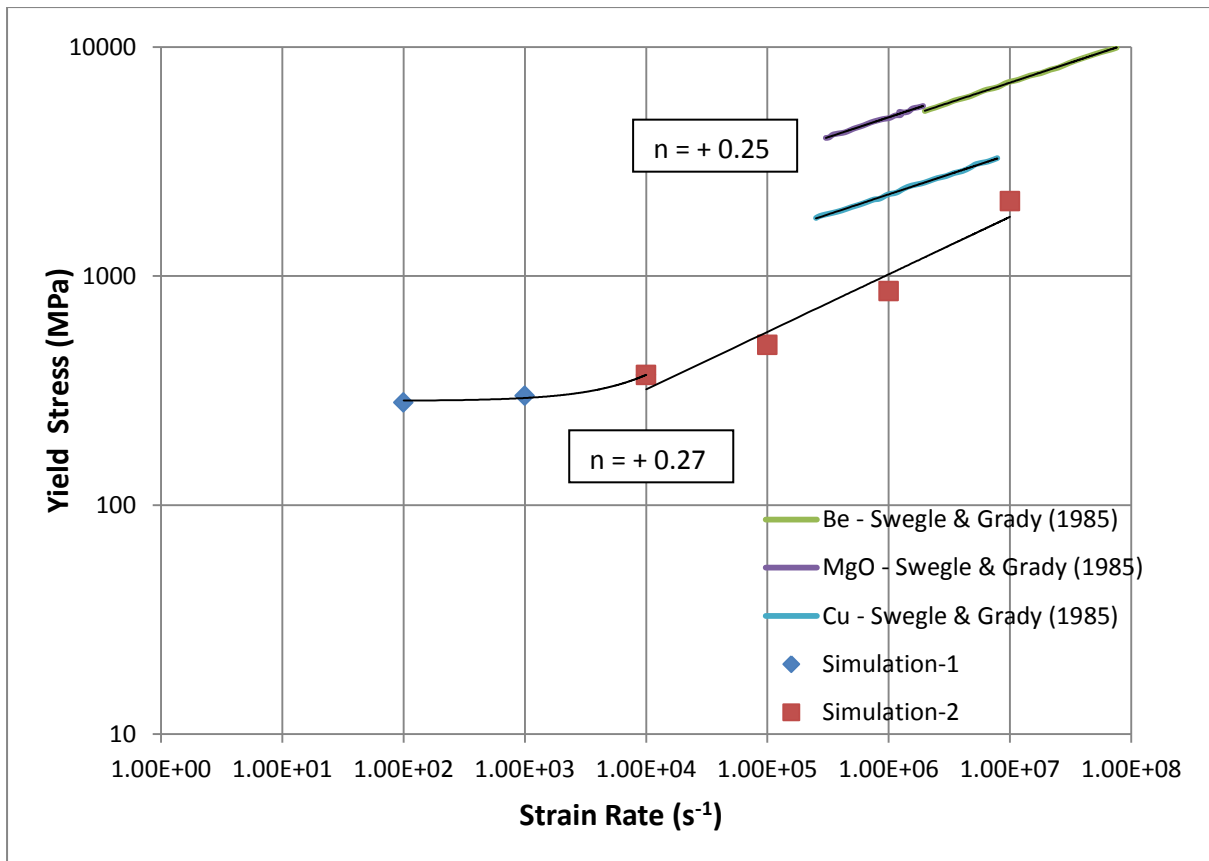Figure 22: Stress-Strain Curves for strain rates for 10^5 to 10^7

Figure 23: Log-log plot of yield stress variation at different strain rates

Figure 24 shows the evolution of stress, total strain and plastic strain with time at 3 different strain rates (10^3, 10^6 and 10^7). The higher yield stress observed for high strain rates is explained with the onset of plasticity (plastic strain). It is noticed that at high strain rates, plastic strain starts to occur at a higher total strain.
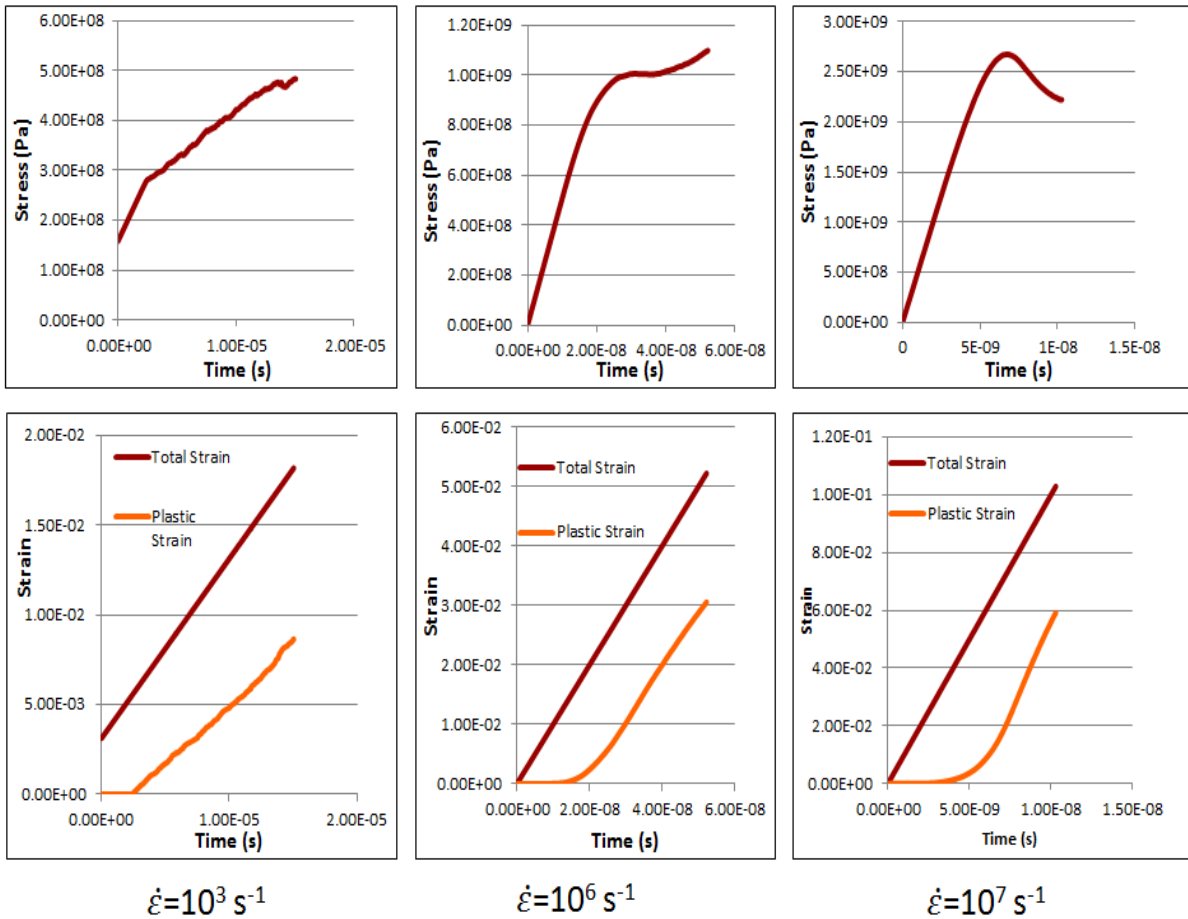
Figure 24: Evolution of stress, total strain and plastic strain with time at 3 different strain rates

The hardening rate is also investigated as a function of strain rate as shown in figure 25. We notice the insensitivity of the hardening rate with variation in the strain rate region $(10^2 - 10^4 \text{ s}^{-1})$ A decrease in the hardening rate is noticed in the higher strain rate region $(10^4 - 10^7 \text{ s}^{-1})$, and a power law exponent of n = - 0.4 is obtained. Usually at higher strain rate, plasticity is established with many mobile dislocations gliding. Thus, the need for the stress to increase is lower, which results in a lower hardening with thermal softening for very high strain rates.
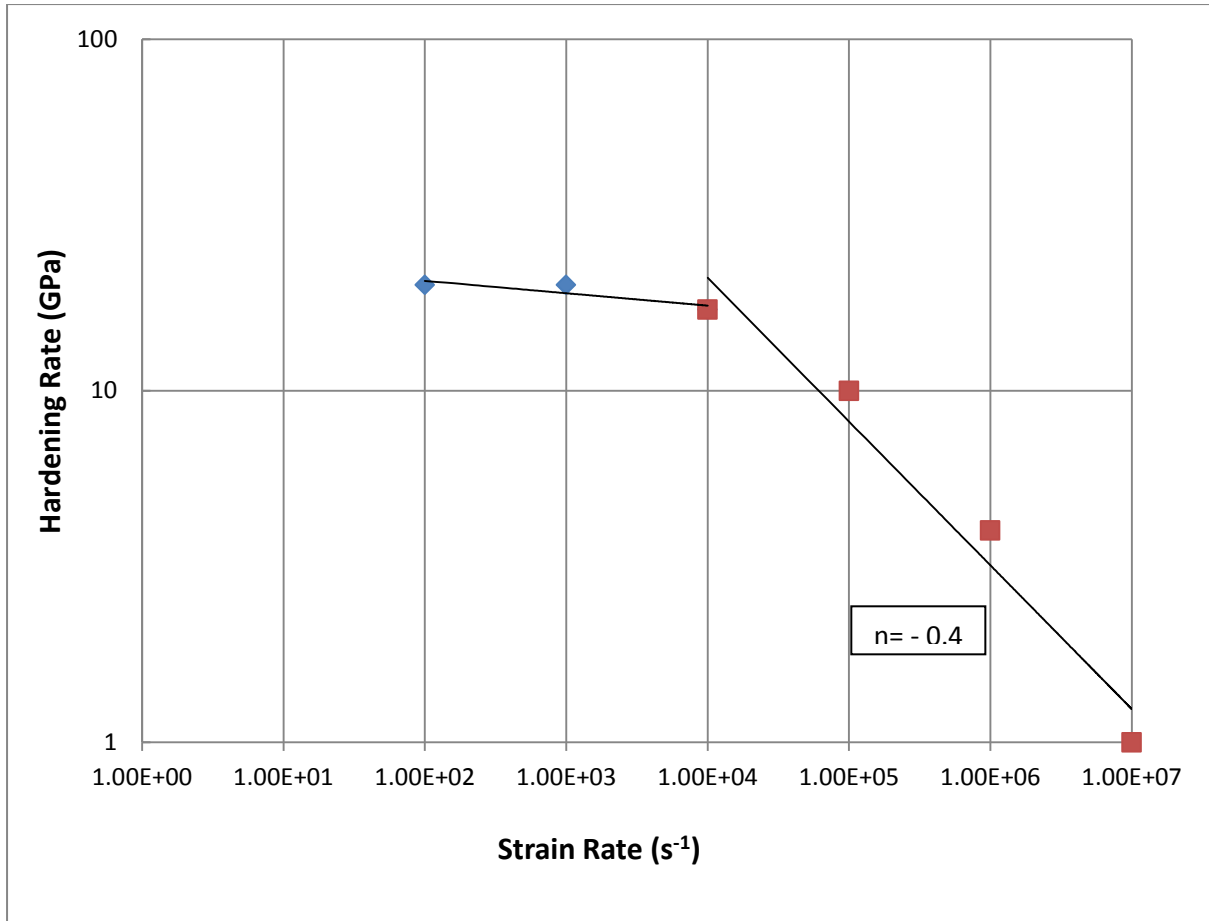
Figure 25: Log-log plot of the hardening rate at different strain rates

Looking into the evolution of dislocation density versus time for different strain rates in figure 26, we notice that following:

- For high strain rates (10^6 - 10^7): steep slope corresponding to very fast rate of dislocation multiplication.

- For strain rates range (10^4 - 10^5): steep slope at the beginning, followed by a short period of dislocation density stability where enough plasticity is generated for relaxation, before density continues to increase again as more sources are activated.

- For lower strain rate (10^3): possesses the lowest slope than the other cases, with overall linear increase in the density corresponding to dislocation gliding and source multiplication.
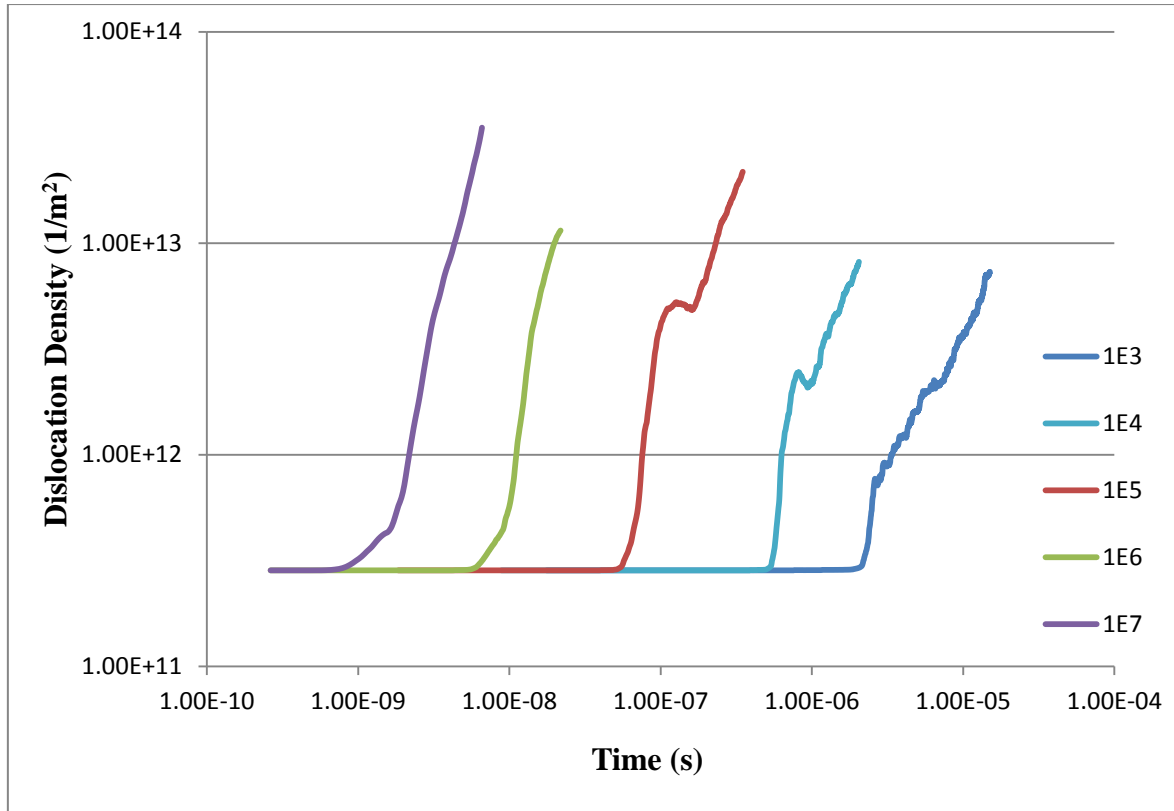
Figure 26: Log-log plot of dislocation density evolution vs. time at different strain rates

3. Shock Loading:

Figure 27 depicts the velocity profile of shock compression experiments along the c-axis of magnesium single crystals for Winey et al. [51] and Garkushin et al. [52]. Figure 28 shows the particle velocity history for our simulations only. Because of difference in time scales between our simulations and experiments, figure 29 shows all three curves together with time normalized. The similarity in the waveform behavior is clear for the three curves with an elastic precursor wave followed by a plastic shock wave. The velocity at the Hugoniot Elastic Limit (HEL) of our simulation (110 m/s) is within the range of experiments (140 m/s and 80 m/s). The higher HEL (140m/s) obtained by Garkushin et al. [52] is expected because of higher saturation velocity (~550 m/s). We notice that the saturation velocity of our simulation (~400 m/s) is in agreement with experiment of Winey et al. [51]. However, the slightly higher HEL value obtained can be attributed to the fact that in their study [51], the

free surface velocity history was measured, while in our simulation, the particle velocity is measured in a small window inside the simulation domain. Considering that the wave decays while propagating, it seems logical to obtain a slightly higher value of the HEL.
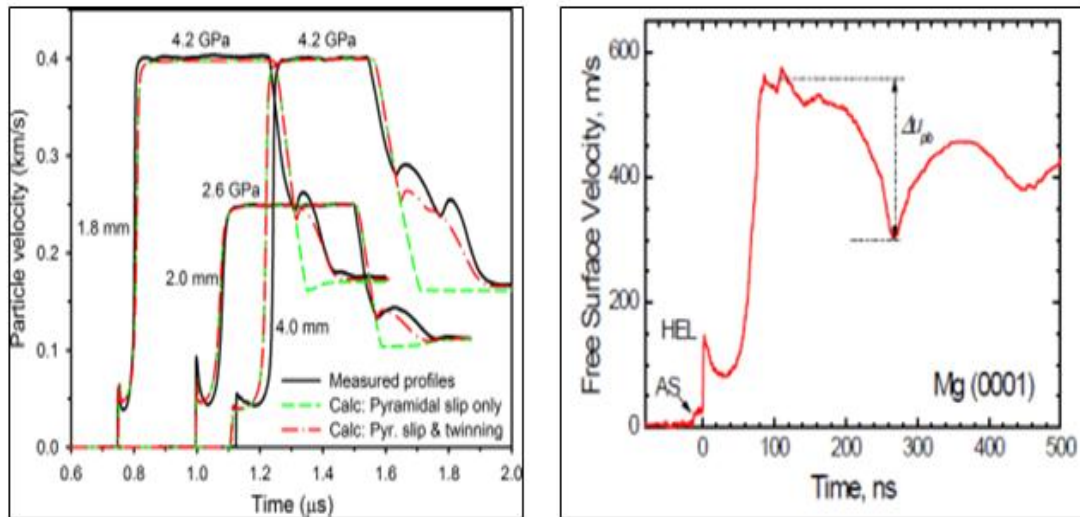

Figure 27: Particle velocity history for shock loading experiments by Winey et al. (Right) and Garkushin et al. (Left)
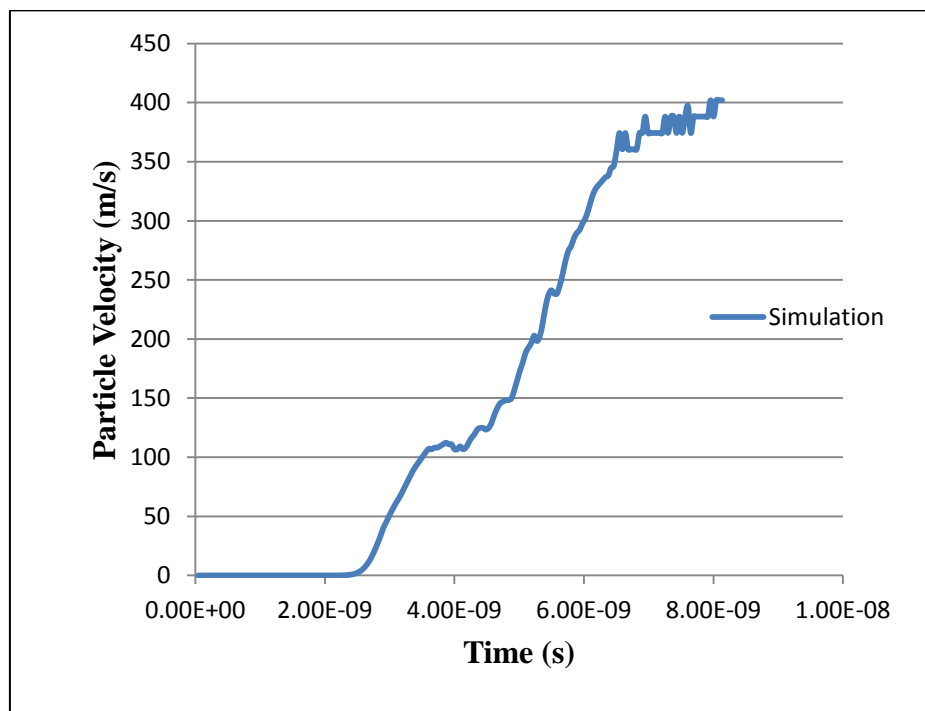

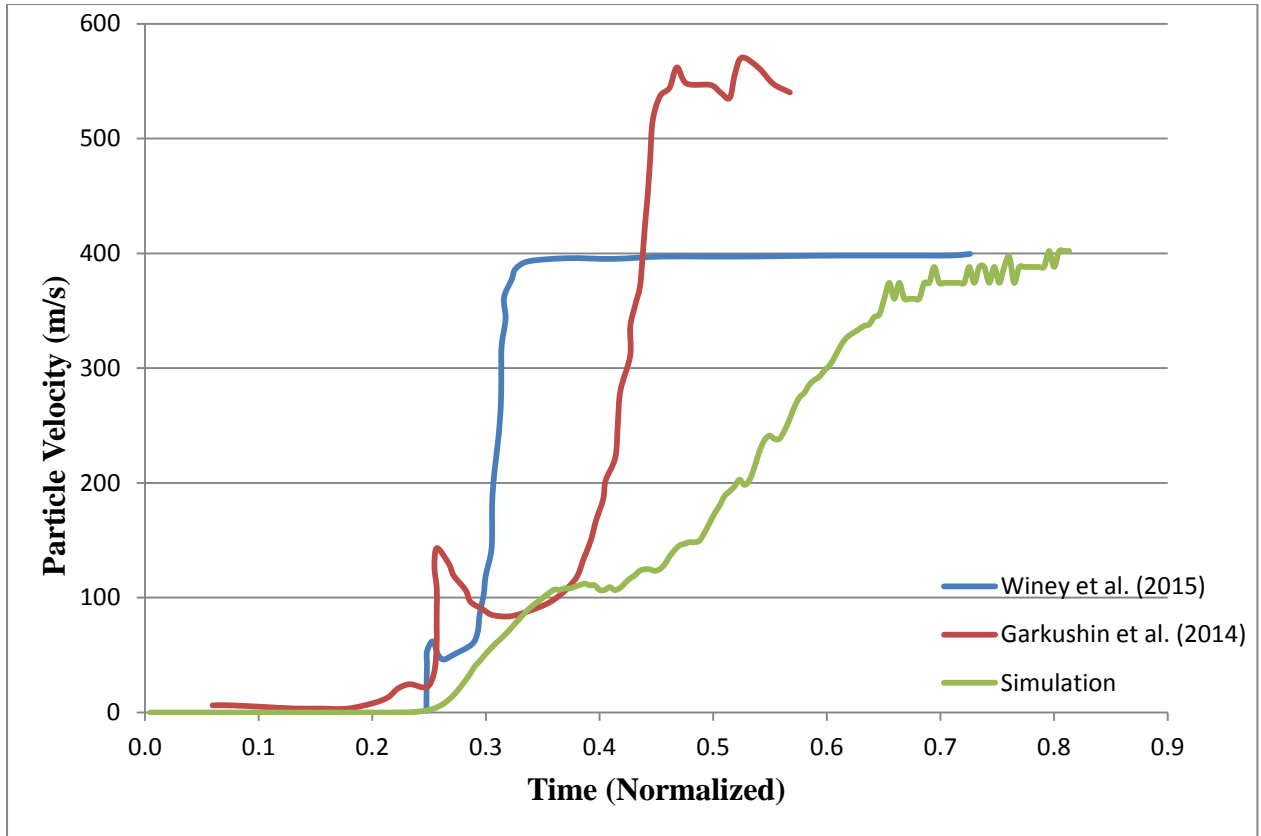Figure 28: Particle velocity history as predicted by our simulations

Figure 29: Particle velocity history for our simulation and data from Winey et al. [51] and Garkushin et al. [52]

Figure 30 depicts the stress vs. the time (normalized) for our simulation and from experiments by Winey et al. [51]. The level of stresses at the HEL is comparable with a higher value for the experimental result. As discussed earlier, the higher peak stress of the experiment (~4.2 GPa) than our simulation (~3.7 GPa) will likely produce a higher HEL stress. In figure 31, the stress profile across the z-axis of the simulation domain is shown at different times. The time shown (up to 5 ns) corresponds to the loading phase of the shock wave. The microevolution of dislocations corresponding to different times is presented in figure 32. At time t_1, the wave propagates pure elastically. At time t_2, the onset of plasticity is seen with a HEL. This corresponds to figure 26 (b), where the wave propagates and plasticity is shown with dislocation gliding. As wave propagates with time, the HEL becomes much clearer with a small ledge formed. We observe that with time, the HEL becomes slightly

lower as the wave decays. At t = 5 ns, the loading phase is near the end, with the steady stress state (Plateau) is reached at ~ 4 GPa. The microstructure in figure 32 (d) corresponds to the time when the wave reaches the end of simulation domain, with huge dislocation motion all over the domain.
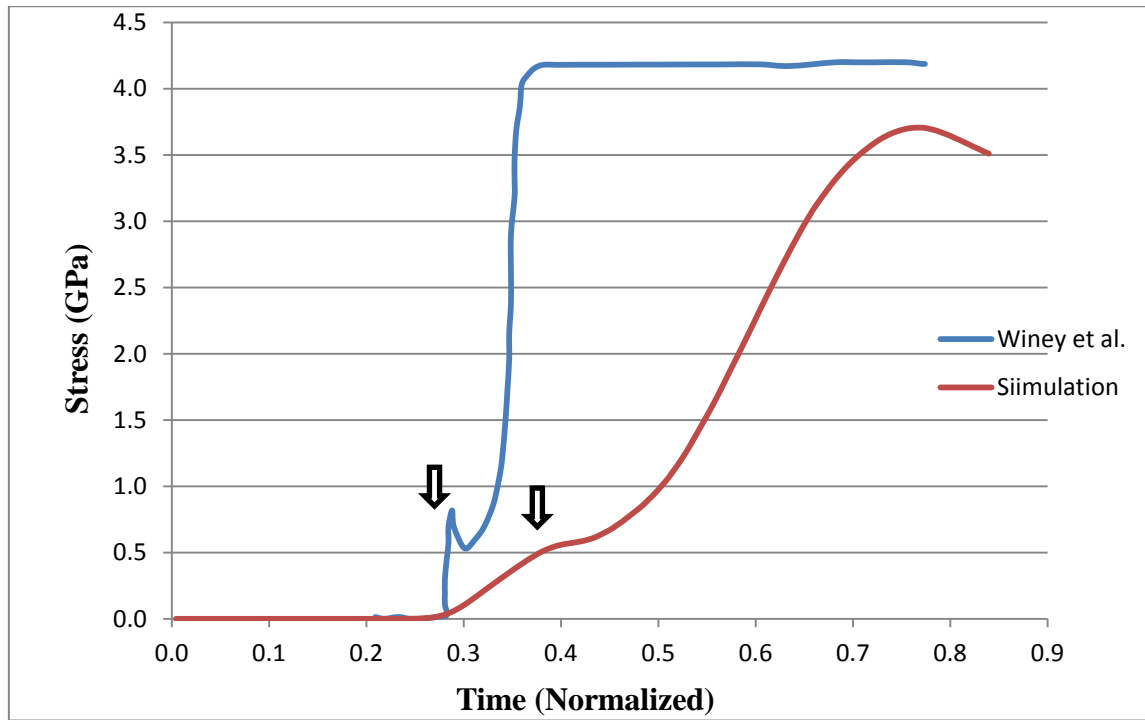

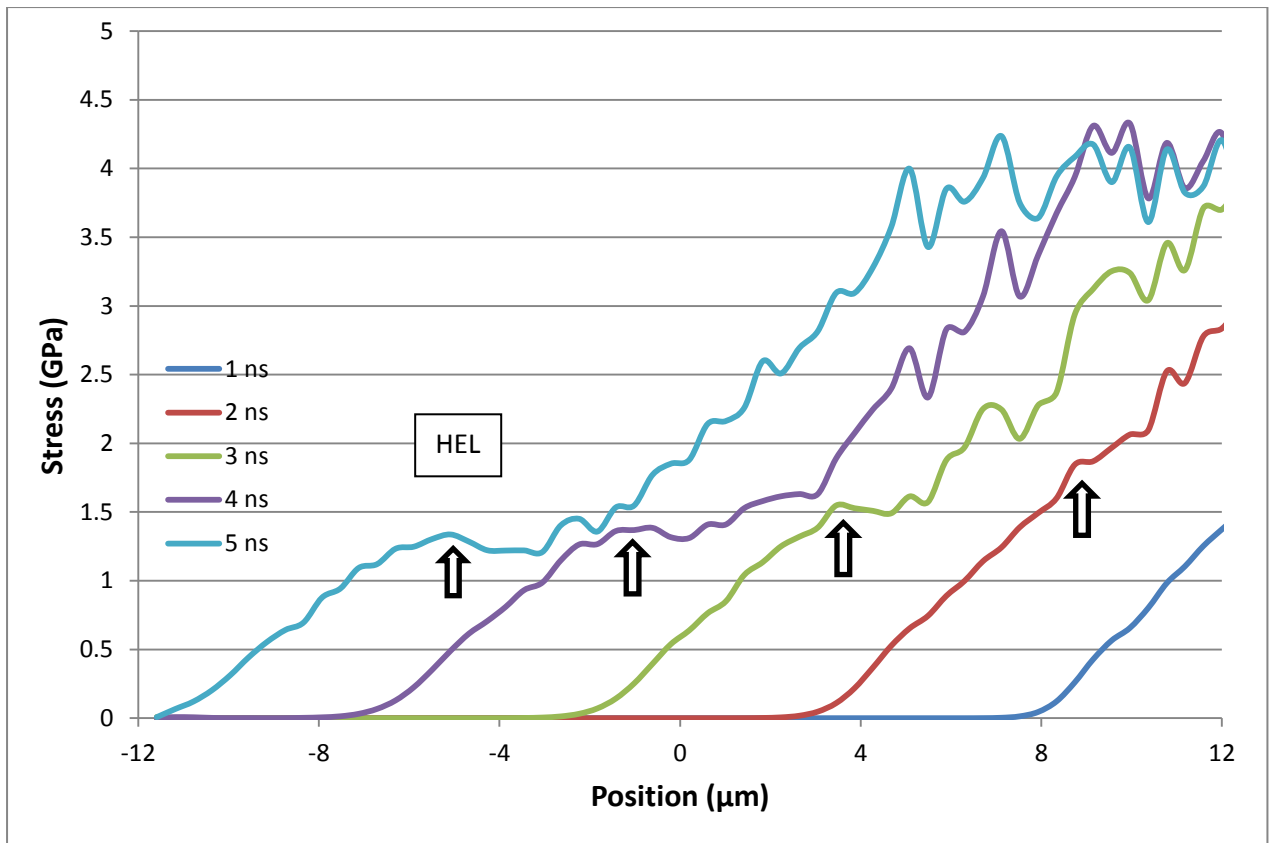Figure 30: Stress vs. time for our simulation and from Winey et al. [51]

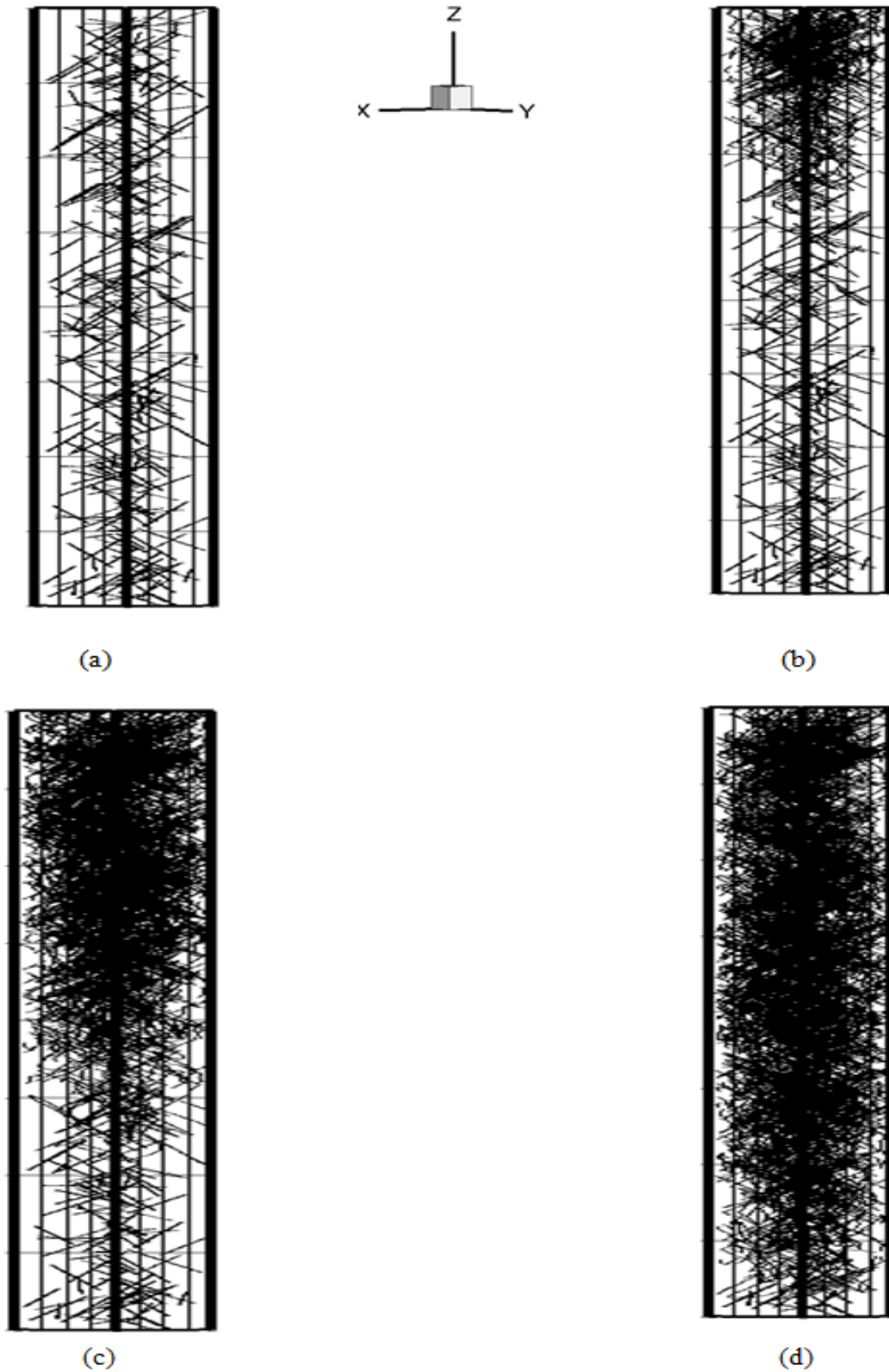Figure 31: Stress profile in the simulation sample at different times

Figure 32: (a) Initial Simulation Setup (b) Evolution of microstructure after start of shock loading (t = 2 ns) (c) Propagation of shock wave (t = 3 ns) (d) Microstructure at the end of loading phase (t = 5 ns)

B. Basal Slip

The simulation setup is similar to the one of pyramidal slip but with crystal oriented for basal slip in the [2$\overline{1}\overline{1}$2] direction. The simulation domain has dimensions of 5 μm × 5 μm × 10 μm. In DD, periodic boundary condition is used to model dislocation motion in bulk crystals. Representative compression stress vs. strain plot is shown in figure 33. The curve shows a similar behavior to the obtained plot of macrocompression tests by Prasad et al. [11] (see figure 34); It is characterized by an easy glide with a slight hardening behavior. The curve assumes a perfectly elastic behavior up to 0.1 %, where a small elastic overshoot is noticed. This can be related to the very low Peierl's stress of the basal slip (0.5 MPa), where the stress to bow out the FR sources controls the yielding process. However, the yield point (at 10-15 MPa) is in the range of macrocompression experiments [8, 9].
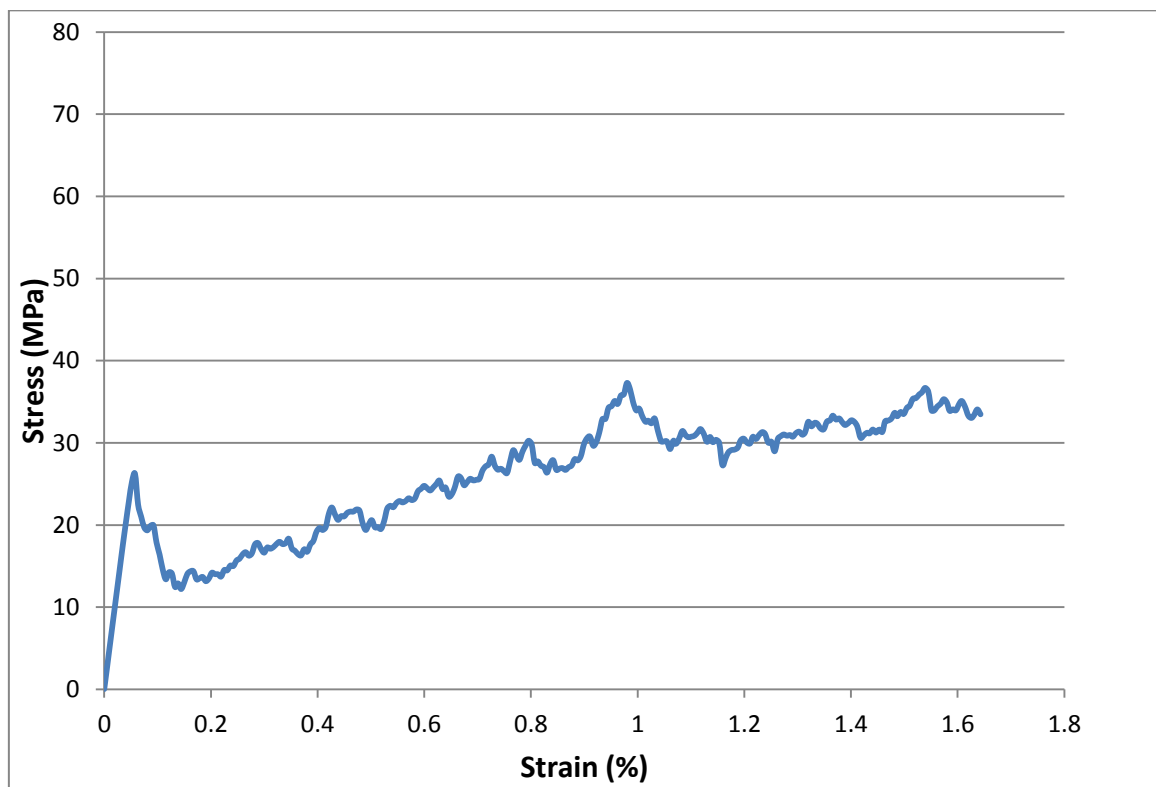
Figure 33: Obtained Stress-Strain Curve for the [2$\overline{1}\overline{1}$2] oriented crystal

53
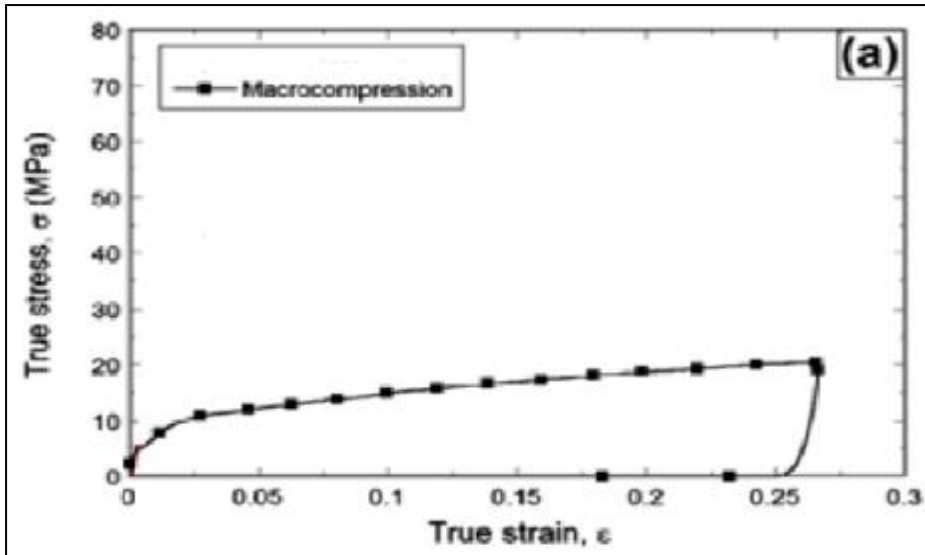
Figure 34: Stress-Strain curve for macrocompression of Mg single crystal by Prasad et al. [11]

Figure 35 shows the evolution of the dislocation density versus time. Similar to the pyramidal slip case, the curve shows three distinct regimes. The first one is a short period at the beginning that corresponds to time when stress is still below the resolved shear stress. With the increase in stress, the abrupt increase in the dislocation density is clear. The process of dislocation emission continues but at a lower rate and another abrupt increase is noticed such that new FR sources are now activated. Eventually, dislocation density saturation is attained with a value of $\sim 3.1 \times 10^{13}$.

Figure 35: Dislocation density evolution versus time

Snapshots of the microstructural evolution of the dislocations in this simulation are shown in figure 29. The beginning of plastic behavior (corresponds to 0.2 % total strain) is shown in figure 29 (a) with the start of bowing out of some sources. Plastic deformation process continues with gliding of dislocations on basal slip; eventually, all FR sources are activated. During the simulated deformation, the flow stress on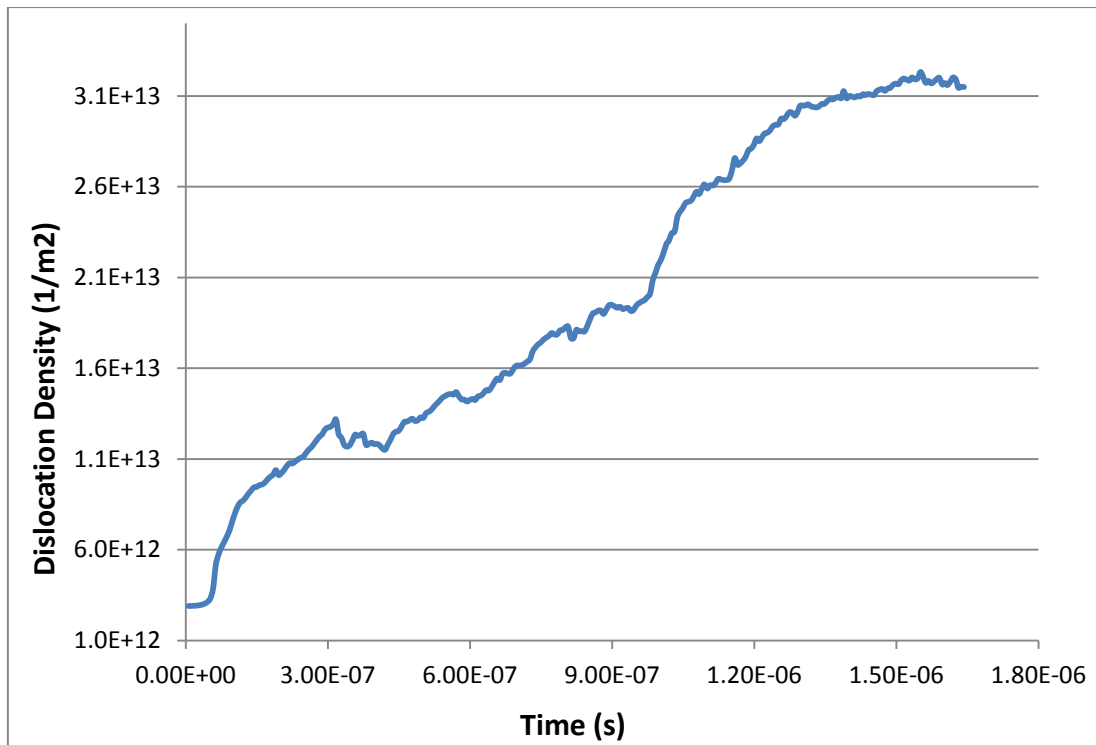 the primary system increases until it reaches a quasi-saturation value. The saturation in the flow stress corresponds to the regime where the imposed strain is entirely accommodated by primary dislocation glide through the forest. However, when this regime is established, fluctuations remain. These are due to interactions between dislocations. For example, when one primary dislocation gets pinned by two forest dislocations, an increase in the flow stress is required for the moving dislocation to overcome this obstacle. At some point, the resolved shear stress becomes high enough such that the dislocation can bow-out or break away from the forest, leading to a decrease in the flow stress as glide is suddenly able to relax the stress that has built up. It is

worth mentioning that according to table 4, for the [2$\overline{11}$2] loading, non-zero Schmid factors are obtained for all slip systems (basal, prismatic and pyramidal). However, as shown in the figure, only FR sources that correspond to basal slip are activated with the other sources remain inactivated. This is due to that fact that in reference to table 8, the peierl's stress of basal slip planes is only 0.5 MPa compared to one order and ten order higher values for prismatic and pyramidal system respectively.
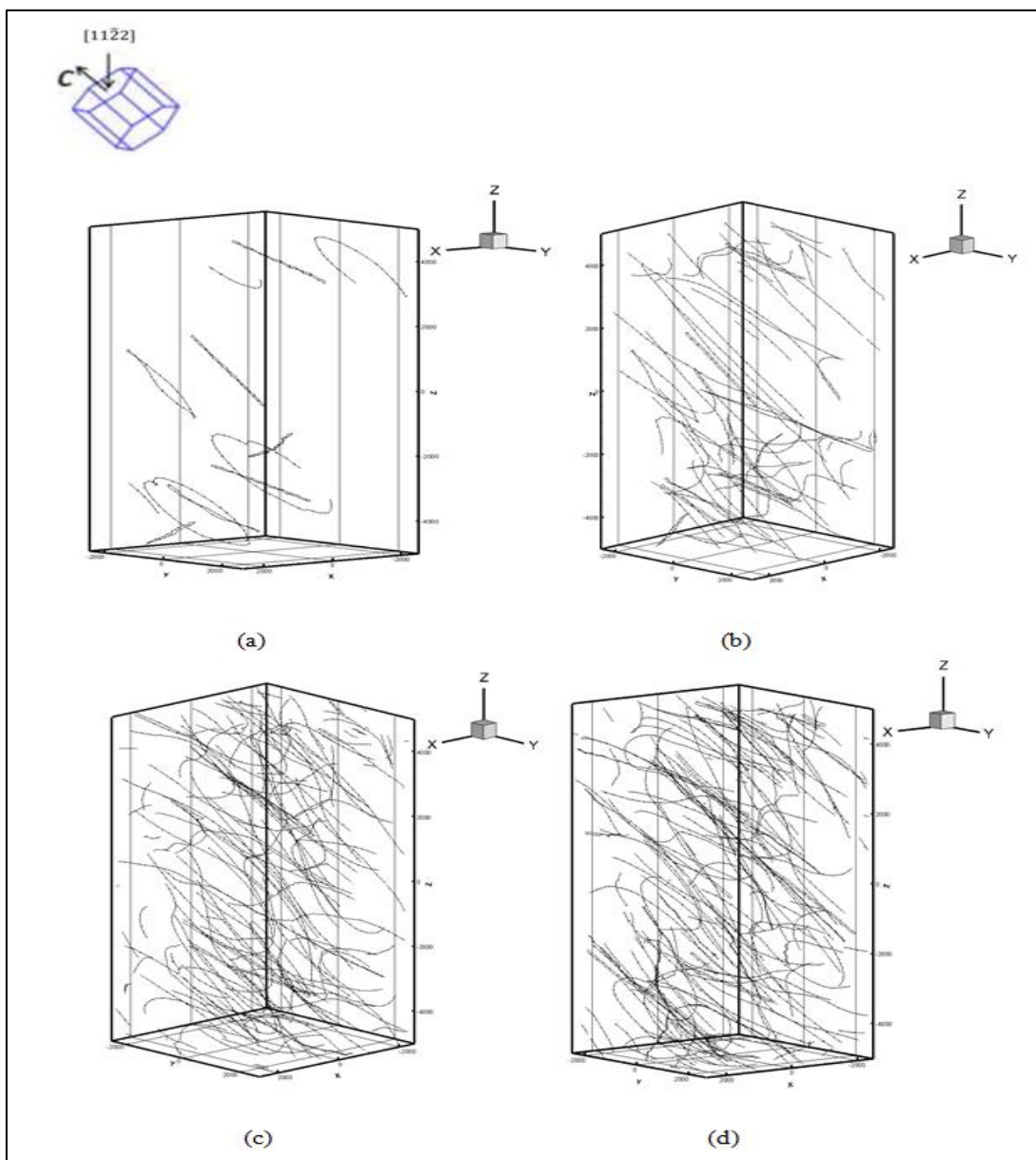

Figure 36: Snapshots of the microstructural evolution for the [2$\overline{11}$2] oriented crystal

Chapter IV

CONCLUSION AND FUTURE WORK

We carried out investigations of the deformation behavior in Mg single crystal using dislocation dynamics simulations. The thesis report starts with a review of the background of the crystallographic information concerning Mg crystals and an overview of the current understanding of the deformation mechanisms is given. Two main orientations were studied: [0001] and [$2\overline{1}\overline{1}2$] that correspond to pyramidal and basal slip respectively. The stress-strain relations resulting from simulations have been presented and discussed in terms of orientation dependent slip activity and the microstructural evolution of dislocations. A parametric study for mobility was performed to investigate the consequence of dislocation mobility dependence on dislocation character. We were able to obtain the hardening behavior, observed in experimental studies, by setting a high mobility value to edge segments and the screw dislocations as stationary. In addition, yield stress and hardening rate were plotted as a function of the simulation sample length, and the exponent was calculated. The observed size effect is in agreement with experimental studies. High strain rate loading is also studied with the variation of yield stress and hardening rate discussed. Regarding shock loading simulations, the particle velocity history, and the stress profile obtained are consistent with recent shock loading experiments.

Finally, we can say that these findings provide better understanding of the complicated plastic deformation in HCP crystals, in particular, Mg single crystals. Amid reports of c-axis compression leading to activation of pyramidal I instead on pyramidal II, an investigation of this issue, in addition to other crystal orientation (particularly prismatic slip), and twinning contribution to deformation behavior may constitute future work in this field.

BIBLIOGRAPHY

[1] Avedesian M, Baker H, editors. ASM specialty handbook, magnesium and magnesium alloys. Materials Park, OH: ASM International;1999.

[2] Li, N., & Zheng, Y. (2013). Novel Magnesium Alloys Developed for Biomedical Application: A Review. Journal of Materials Science & Technology.

[3] Hull, D., & Bacon, D. J. (2011). *Introduction to dislocations* (Vol. 37). Elsevier.

[4] Partridge, P. G. (1967). The crystallography and deformation modes of hexagonal close-packed metals. International Materials Reviews, 12(1), 169-194.

[5] E.C. Burke and W.R. Hilbbard, Jr., J. Metals, Trans. AIME 194 (1952) p.295.

[6] B. C. Wonsiewicz and W. A. Backofen: Trans. TMS-AIME, 1967, vol. 239, p. 1422.

[7] Hirsch P.B and Lally J.S 1965, Phil Mag., 12, 595.

[8] Seok Kim, G. (2011). Small volume investigation of slip and twinning in magnesium single crystals (Doctoral dissertation, Université de Grenoble).

[9] Bhattacharya, B., &Niewczas, M. (2011). Work-hardening behavior of Mg single crystals oriented for basal slip. Philosophical Magazine, 91(17), 2227-2247.

[10] Yoshinaga, H., Horiuchi, R., 1963. On the nonbasal slip in magnesium crystals. Trans. Jpn. Inst. Met. 5, 14–21.

[11] Prasad, K. E., Rajesh, K., &Ramamurty, U. (2014). Micropillar and macropillar compression responses of magnesium single crystals oriented for single slip or extension twinning. ActaMaterialia, 65, 316-325.

[12] Aitken, Z. H., Fan, H., El-Awady, J. A., & Greer, J. R. (2015). The effect of size, orientation and alloying on the deformation of AZ31 nanopillars. *Journal of the Mechanics and Physics of Solids*, *76*, 208-223.

[13] Couret, A., &Caillard, D. (1985). An in situ study of prismatic glide in magnesium—I.The rate controlling mechanism.ActaMetallurgica, 33(8), 1447-1454.

[14] Reed-Hill, R.E., Robertson, W.D., 1957. Deformation of magnesium single crystals by nonbasal slip. Transactions of AIME 209, 496-502.

[15] Molodov, K. D., Al-Samman, T., Molodov, D. A., & Gottstein, G. (2013). On the Ductility of Magnesium Single Crystals at Ambient Temperature. Metallurgical and Materials Transactions A, 1-7.

[16] Li, Q. (2013). Microstructure and deformation mechanism of 0001 magnesium single crystal subjected to quasistatic and high-strain-rate compressive loadings. Materials Science and Engineering: A, 568, 96-101.

[17] Taylor GI., Plastic strain in metals. *J. Inst. Met.,* 1938:62:307.

[18] Obara, T., Yoshinga, H., Morozumi, S., 1973. {11-22}<1-1 23> slip systems in magnesium. ActaMetellurgica 21, 845-853.

[19] Stohr, J. F. and J. P. Poirier (1972). "Etude enMicroscopieElectronique de Glissement Pyramidal {11-22} <11-23>dans le Magnesium." Philosophy Magzine 25: 1313-1329.

[20] Byer CM., Li B., Cao B., Ramesh KT., Microcompression of single-crystal magnesium, Scripta Mater., 2010:62:536

[21] Lilleodden, E. (2010). Microcompression study of Mg (0001) single crystal.ScriptaMaterialia, 62(8), 532-535.

[22] Ando S, Nakamura K, Takashima K and Tonda H,1992, J.Japan Inst. of light metals, 42,2845.

[23] Ando, S. and H. Tonda (2000). "Non-Basal Slip in Magnesium-Lithium Alloy Single Crystals." Materials Transactions, JIM 41(9): 1188-1191.

[24] Ando, S., Tsushida, M., &Kitahara, H. (2010, October). Deformation Behavior of Magnesium Single Crystal in c-axis Compression and a-axis Tension. In Materials Science Forum (Vol. 654, pp. 699-702).

[25] Chapuis, A., & Driver, J. H. (2011). Temperature dependency of slip and twinning in plane strain compressed magnesium single crystals. ActaMaterialia, 59(5), 1986-1994

[26] Li, Q. (2011). Dynamic mechanical response of magnesium single crystal under compression loading: Experiments, model, and simulations. Journal of Applied Physics, 109(10), 103514.

[27] Syed, B., Geng, J., Mishra, R. K., & Kumar, K. S. (2012). [0001] Compression response at room temperature of single-crystal magnesium.ScriptaMaterialia, 67(7), 700-703.

[28] Monnet, G., Devincre, B., &Kubin, L. P. (2004). Dislocation study of prismatic slip systems and their interactions in hexagonal close packed metals: application to zirconium. Actamaterialia, 52(14), 4317-4328.

[29] Guo, Y., Tang, X., Wang, Y., Wang, Z., & Yip, S. (2013). Compression deformation mechanisms at the nanoscale in magnesium single crystal. ActaMetallurgicaSinica (English Letters), 26(1), 75-84.

[30] J. Geng, M.F. Chisholm, R.K. Mishra & K.S. Kumar (2014) The structure of ⟨c + a⟩ type dislocation loops in magnesium, Philosophical Magazine Letters, 94:6, 377-386

[31] Groh, S., Marin, E. B., Horstemeyer, M. F., & Bammann, D. J. (2009). Dislocation motion in magnesium: a study by molecular statics and molecular dynamics. *Modelling and Simulation in Materials Science and Engineering*, *17*(7), 075009.

[32] Caillard, D., & Couret, A. (2002). Dislocation movements controlled by friction forces and local pinning in metals and alloys. *Materials Science and Engineering: A*, *322*(1), 108-117.

[33] Capolungo, L. (2011). Dislocation junction formation and strength in magnesium. *Acta Materialia*, *59*(8), 2909-2917.

[34] Madec R, Kubin L. Scripta Mater 2008;58:767–70.

[35] Ghazisaeidi, M., Hector, L. G., & Curtin, W. A. (2014). First-principles core structures of< c+ a> edge and screw dislocations in Mg. *Scripta Materialia*, *75*, 42-45.

[36] Shin, I., & Carter, E. A. (2014). Simulations of dislocation mobility in magnesium from first principles. *International Journal of Plasticity*, *60*, 58-70.

[37] Meyers, M. A., 1994, *Dynamic Behavior of Materials*, (New York: John Wiley & Sons), p. 119.

[38] H.M. Zbib and T.D. de la Rubia, Int. J. Plast. 18 (2002) p.1133.

[39] J.P. Hirth, H.M. Zbib and J. Lothe, Model. Simulat.Mater.Sci. Eng. 6 (1998) p.165.

[40] M.A. Shehadeh Phil. Mag. 92 (2012) p.1173.

[41] Staroselsky, A., &Anand, L. (2003). A constitutive model for hcp materials deforming by slip and twinning: application to magnesium alloy AZ31B. International Journal of Plasticity, 19(10), 1843-1864.

[42] Long, T. R., & Smith, C. S. (1957). Single-crystal elastic constants of magnesium and magnesium alloys. ActaMetallurgica, 5(4), 200-207.

[43] Tang, Y., & El-Awady, J. A. (2014). Highly anisotropic slip-behavior of pyramidal I< c+ a> dislocations in hexagonal close-packed magnesium. Materials Science and Engineering: A, 618, 424-432.

[44] Norfleet DM., Dimiduk DM., Polasik SJ., Uchic MD., Mills MJ., Dislocation structures and their relationship to strength in deformed nickel microcrystals, Acta Mater., 2008:56:2988.

[45] Greer JR., Nix WD., Nanoscale gold pillars strengthened through dislocation starvation, *Phys. Rev. B,* 2006;73:245410.

[46] Byer, C. M., & Ramesh, K. T. (2013). Effects of the initial dislocation density on size effects in single-crystal magnesium.ActaMaterialia, 61(10), 3808-3818.

[47] Prasad, K. E., Li, B., Dixit, N., Shaffer, M., Mathaudhu, S. N., & Ramesh, K. T. (2014). The Dynamic Flow and Failure Behavior of Magnesium and Magnesium Alloys. *JOM*, *66*(2), 291-304.

[48] Tucker, M. T., Horstemeyer, M. F., Gullett, P. M., El Kadiri, H., & Whittington, W. R. (2009). Anisotropic effects on the strain rate dependence of a wrought magnesium alloy. *Scripta Materialia*, *60*(3), 182-185.

[49] Dixit, N., Xie, K. Y., Hemker, K. J., & Ramesh, K. T. (2015). Microstructural evolution of pure magnesium under high strain rate loading. *Acta Materialia*, *87*, 56-67.

[50] Swegle, J. W., & Grady, D. E. (1985). Shock viscosity and the prediction of shock wave rise times. *Journal of applied physics*, *58*(2), 692-701.

[51] Winey, J. M., Renganathan, P., & Gupta, Y. M. (2015). Shock wave compression and release of hexagonal-close-packed metal single crystals: Inelastic deformation of c-axis magnesium. *Journal of Applied Physics*, *117*(10), 105903.

[52] Garkushin, G. V., Savinykh, A. S., Kanel, G. I., Razorenov, S. V., Jones, D., Proud, W. G., & Botvina, L. R. (2014, May). Response of magnesium single crystals to shock-wave loading at room and elevated temperatures. In *Journal of Physics: Conference Series* (Vol. 500, No. 11, p. 112027). IOP Publishing.